Structural and electrical properties of RSbTe (R = La, Y) nodal-line semimetals with tunable band filling

Haruka Kageyama, Atsushi Maebara, Yoshio Nogami, and Ryusuke Kondo [*]

Department of Physics, Okayama University, Okayama 700-8530, Japan

RSbTe (R = rare earth) compounds belong to the ZrSiS-type material family, characterized by a square lattice that hosts topological nonsymmorphic Dirac fermions and nodal-line fermions owing to its high crystalline symmetry. In this study, we investigate the structural and electrical properties of the nonmagnetic RSbTe compounds, LaSbTe and YSbTe, achieving precise control of their band fillings through a crystal growth technique that enables fine-tuning of the Te/Sb ratio. We show that, in the Te-rich region, both compounds crystallize in a high-symmetry tetragonal phase. In this phase, LaSbTe exhibits charge-density-wave order accompanied by a distortion into an orthorhombic lattice, consistent with previous reports. In the Sb-rich region of both compounds, the structure transforms into an orthorhombic phase with space group $P2_12_12_1$ (No. 19), featuring a distorted kite-shaped square lattice. This phase exhibits a narrow energy gap, which we attribute to remnants of the band crossings present in the tetragonal phase. We clarify the crystal structures including instabilities arising from high crystalline symmetry, electronic structures, and electrical properties. These findings provide a foundation for future studies of RSbTe systems, particularly on the interplay between nontrivial band topology and magnetism induced by lanthanide substitution.

I. INTRODUCTION

Since the discovery of three-dimensional topological insulators such as $Bi_{1-x}Sb_x$ and Bi_2Se_3 [1–6], the study of topological materials has attracted significant attention in condensed matter physics [7–14]. Unlike conventional materials, topological materials host electronic states protected by the topology of their electronic band structures, rendering them robust against perturbations. For instance, topological insulators exhibit robust gapless surface states—characterized by ultrahigh carrier mobility and spin polarization—coexisting with an insulating bulk [7–9]. Following these discoveries, the concept of electronic band topology has been extended to a variety of other material classes, including topological superconductors [8,10,11], semimetals [12,13], and topological crystalline insulators [10,14].

Among these, topological semimetals have emerged as a particularly active area of research. They exhibit topologically protected band crossings in their electronic structures, i.e., in momentum space. These materials are classified based on the shape of these band crossings: topological semimetals with pointlike degeneracies are categorized as Dirac semimetals [15–21] or Weyl semimetals [22–29], while those with continuous one-dimensional linelike crossings are referred to as nodal-line semimetals [30–34]. They have been predicted to exhibit a wide range of exotic physical properties, some of which have already been experimentally observed [35,36], such as ultrahigh carrier mobility [37–39] extremely large, nonsaturating magnetoresistance [40–43], and negative magnetoresistance arising from the chiral anomaly [44–49].

Although nodal-line semimetals were initially less explored compared with Dirac and Weyl semimetals, interest in them has grown rapidly following the discovery of a nodal-line electronic structure in ZrSiS [50–53] and in RSbTe (R = rare earth) compounds, which share the same crystal structure as ZrSiS [54] and have recently attracted significant attention. This interest arises from the fact that magnetic rare-earth elements can easily introduce magnetism into the RSbTe system. Such magnetic incorporation is expected to induce new physical phenomena resulting from the interplay between magnetism and topological electronic states, as well as from modifications of the topological characteristics of the electronic states caused by symmetry changes associated with magnetic ordering.

Numerous studies of RSbTe have been reported to date [55]. RSbTe, where R ranges from La to Ho [56], has been confirmed to host topological nodal-line electronic structures, as revealed by ARPES [57–68]. Several of these compounds have also been identified as topological nodal-line semimetals based on first-principles calculations and transport measurements [69–75]. Most of the magnetic compounds exhibit antiferromagnetic orderings at low temperatures, and some display distinct magnetic features such as steplike magnetization curves [74,76] and signatures of Kondo localization [63,70,71,77]. Notably, CeSbTe has been found to host various topological semimetal states, including multifold Dirac and Weyl crossings, which can be readily tuned by controlling the magnetic state via temperature or external magnetic fields [58]. Moreover, field-induced changes in the electronic structure of the magnetic states of HoSbTe have been directly observed using scanning tunneling microscopy [78].

These studies suggest that RSbTe is a promising platform for exploring exotic phenomena arising from the correlated

---

[*] Contact author: ryusuke.kondo@okayama-u.ac.jp

interplay between topologically protected electronic states and magnetism. Such phenomena are of particular interest for next-generation technological applications, including spintronics. However, to effectively utilize these phenomena for technological applications, precise control of band filling is essential. This is because these remarkable properties will emerge when the topologically protected band crossings, i.e., Dirac/Weyl points or nodal line, lie at the Fermi level. Indeed, band-filling control has been recognized as a key factor in achieving distinctive bulk electronic properties in other topological semimetal systems [79]. In contrast, only limited studies have focused on the control of band filling in the RSbTe system [76], with a few exceptions such as studies on GdSbTe [80–82] and NdSbTe [83], which have been confined to the Te-rich region. This is despite reports indicating that variations in the Te/Sb ratio in RSbTe can readily shift the Fermi level [84].

In this work, we report the structural and electrical properties of the nonmagnetic nodal-line semimetals RSbTe ($R =$ La, Y) under continuous band-filling control and examine the resulting electronic structures and electrical behaviors. Single crystals of RSb$_{1-x}$Te$_{1+x}$ ($R =$ La, Y) were successfully synthesized using a simplified crystal growth method, enabling highly reproducible and precise tuning of the band filling across both the Te-rich and Sb-rich regions, centered around the stoichiometric composition RSb$_1$Te$_1$. In the Te-rich region ($x > 0$), the compounds primarily adopt a tetragonal crystal structure, and LaSbTe exhibits charge-density-wave (CDW) order accompanied by a lowering of the symmetry. In contrast, in the Sb-rich region ($x < 0$), the structural transitions to an orthorhombic phase with space group $P2_12_12_1$ (No. 19), which exhibits double periodicity along the stacking axis. We systematically present and discuss the dependence of structural and electrical properties on the nominal synthesis composition. Our findings reveal that the structural and electrical properties of RSbTe compounds are highly sensitive to their composition and that precise single-crystal structural analysis is essential for an accurate understanding of their electronic characteristics.

II. EXPERIMENTAL PROCEDURES

All compounds were synthesized using the conventional self-flux method. Starting materials, rare-earth (R) elements (lanthanum [La], (99.9% Kojundo Chemical Lab. Co., Ltd.), yttrium [Y], (99.9% Kojundo Chemical Lab. Co., Ltd.)), antimony (Sb, 99.999% Kojundo Chemical Lab. Co., Ltd.), and tellurium (Te, 99.999% Furuuchi Chemical Corporation), were weighed, mixed, and loaded into an alumina crucible. The crucible was sealed in a quartz ampoule under an argon atmosphere to prevent Te evaporation during the reaction. The sealed ampoule was heated to 1373 K over 24 h and held at that temperature to ensure homogeneous mixing of the ingredient materials. Then it was slowly cooled to 923 K at a rate of 2 K/h, followed by centrifuging to separate the crystals from the excess Sb. Typically, rectangle-shaped crystals with a metallic luster were obtained.

In this study, we found that the Sb-flux method, when combined with careful control of the R to Te ratio, is effective for synthesizing RSbTe samples with controlled band filling.

In this series of studies, the amount of Sb used was typically an order of magnitude greater than that of the R element. This effectiveness is attributed to the difference in electronegativity between Te and Sb. Te, having a higher electronegativity than Sb, preferentially forms bonds with R atoms. When Te is in excess relative to R, the surplus Te atoms, after completing the formation of the [R-Te] slab, are incorporated into the conductive Sb layer, resulting in a higher Fermi level. In contrast, when the amount of Te is insufficient to fully form the [R-Te] slab, Sb atoms substitute into the slab, resulting in a lowering of the Fermi level.

By using scanning electron microscopy with energy-dispersive x-ray spectroscopy (SEM-EDX) analysis, we confirmed that the actual compositions varied depending on the nominal compositions used for synthesis, although the precise compositions could not be determined because of overlapping peaks from multiple elements within a narrow energy range. Therefore, throughout this study, sample compositions are primarily described in terms of the nominal preparation ratios, specifically the R-to-Te ratio used during synthesis.

Crystal structure analyses were performed using Vali-Max with Saturn-HyPix (Rigaku CO.) with Mo K_α. Satellite reflections were also studied during the structure determination process. Precise lattice parameters were determined using a conventional four-circle x-ray diffractometer for single-crystal structure analysis, AFC7R (Rigaku Co.) with Mo K_α. Crystal structures were visualized using VESTA software [85].

First-principles band structure calculations, based on our single-crystal x-ray diffraction (XRD) results, were primarily performed using the full-potential linearized augmented plane wave (FP-LAPW) method implemented in the WIEN2k software package [86]. The exchange correlation of Perdew, Burke, and Ernzerhof within generalized gradient approximation (PBE-GGA) was applied in the calculations. The atomic sphere radius R_{MT} for R atoms, Sb and Te were 2.5 bohr. The truncation of the modulus of the reciprocal lattice vector K_{max} was set to $R_{MT} K_{max} = 7.00$. The k-mesh grid of the Brillouin zone (BZ) was set to 10000. The effect of spin-orbit coupling (SOC) was included in a second-variational procedure step using the scalar-relativistic orbitals as a basis. Electronic structures were calculated both with and without SOC. Calculated Fermi surfaces were visualized using Xcrysden [87]. Band crossings in the electronic structures were searched using the software package WannierTools [88] interfaced with WIEN2k via wien2wannier [89] and wannier90 codes [90].

In-plane electrical resistivity was measured using the conventional four-probe method. The temperature dependence of the resistivity was measured for each sample using a commercial 4KGM Cryocooler (Nagase Sangyo) over the temperature range from room temperature down to approximately 6 K.

III. RESULTS AND DISCUSSION

We first present the results for LaSbTe, followed by those for YSbTe. The results for LaSbTe are categorized according to its crystal structure: the tetragonal phase obtained in the Te-rich region and the orthorhombic phase observed in the Sb-rich region. Hereafter, we refer to these phases as
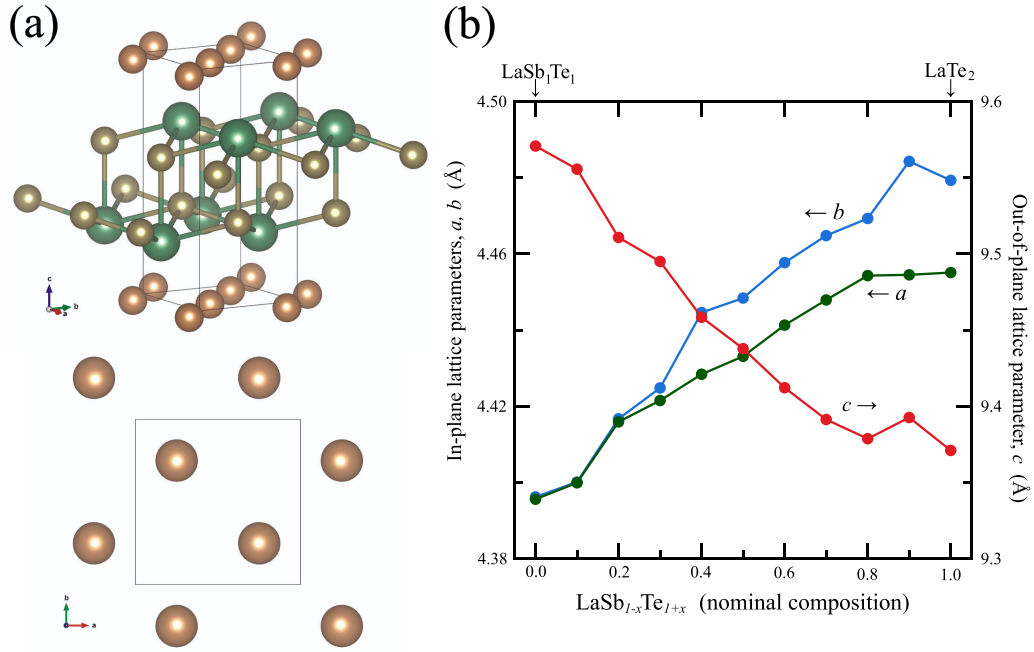
FIG. 1. (a) Crystal structure of 1c-structured LaSbTe (top) and the Sb square net (bottom) and (b) dependence of the lattice parameters of 1c-structured LaSbTe on the nominal composition. The composition labeled $LaTe_2$ in the graph corresponds approximately to the actual composition $LaSb_{0.5}Te_{1.5}$ (see text).

1c-structured LaSbTe and 2c-structured LaSbTe, respectively. The validity of our synthesis method is demonstrated in the section on 1c-LaSbTe by comparing our results with those of a previous study [84], which reported in detail the structural properties of Te-riched $LaSb_{1-x}Te_{1+x}$.

A. LaSbTe

1. 1c-LaSbTe, tetragonal form in Te-rich region

The crystal structure of 1c-LaSbTe is shown in Fig. 1(a). The 1c-LaSbTe samples, which adopted a tetragonal form with a precise square lattice, were obtained within the preparation composition range $0 \leqslant x \leqslant 1$ in $LaSb_{1-x}Te_{1+x}$, corresponding to the Te-rich region. Attempts to prepare samples with $x > 1$, where the preparation ratio of Te to La was larger than 2:1, yielded only small and poor-quality crystals. The structure consists of alternating [La–Te] slabs and Sb square nets. A charge-density wave (CDW) formed on the Sb square net above room temperature, leading to a symmetry-lowering structural transition. Consequently, 1c-LaSbTe adopted an orthorhombic lattice at room temperature.

Figure 1(b) shows the dependence of the lattice parameters on the nominal composition. At $x = 0$, the lattice parameters of $LaSb_1Te_1$ are in excellent agreement with previously reported values within experimental error ($a = b = 4.396$ Å, $c = 9.5708$ Å) [57,69]. As the Te concentration on the preparation composition increases, the in-plane lattice parameters a and b increase monotonically, while the out-of-plane parameter c continuously decreases. These trends exhibit a gradual variation in the actual stoichiometry of the grown crystals, consistent with previous findings by E. DiMasi *et al.* [84].

Figures 2(a)–2(f) demonstrate CCD images obtained during crystal structure analyses at room temperature for samples with various nominal compositions. For $x = 1.0$, superlattice spots corresponding to a CDW with a wave vector of approximately 0.25 are observed [Fig. 2(a)]. At $x = 0.6$, the wave vector decreases to 0.2 [Fig. 2(b)]. As shown in Fig. 2(c), the CDW component along the stacking (out-of-plane) axis is 0, indicating that the CDW is two-dimensional in nature and confined within the Sb conducting plane. The lower panels display CCD images of samples prepared with compositions near the stoichiometric one ($x = 0.2, 0.1$, and 0.0). These results indicate the presence of a CDW with a very short wave vector $\leqslant 0.1$ even near the stoichiometric composition, $LaSb_1Te_1$. Figure 2(g) summarizes the dependence of the CDW wave vector on the nominal composition. As the Te concentration decreases and the composition approaches $x = 0.0$, the CDW wave vector decreases. This trend is consistent with the results previously reported by E. DiMasi *et al.* [84], although they did not report the existence of CDWs near the stoichiometric composition.

Here, we discuss the actual composition of the measured samples in order to evaluate the effectiveness of our sample synthesis method. DiMasi *et al.* [84] reported in detail the structural properties of Sb-doped $LaTe_{2-x}Sb_x$ (i.e., Te-rich $LaSb_{1-x}Te_{1+x}, 0 \leqslant x$), including the composition dependence of the lattice parameters and the CDW wave vector. In comparison with their results, we estimate the actual composition of the nominal $LaTe_2$ sample, i.e., $LaSb_{1-x}Te_{1+x}$ at $x = 1.0$.

The nominal $LaTe_2$ sample exhibits a CDW wave vector of about 0.25 and lattice parameters of $a = 4.45$ Å, $b = 4.48$ Å, and $c = 9.37$ Å. Based on the reported correlation
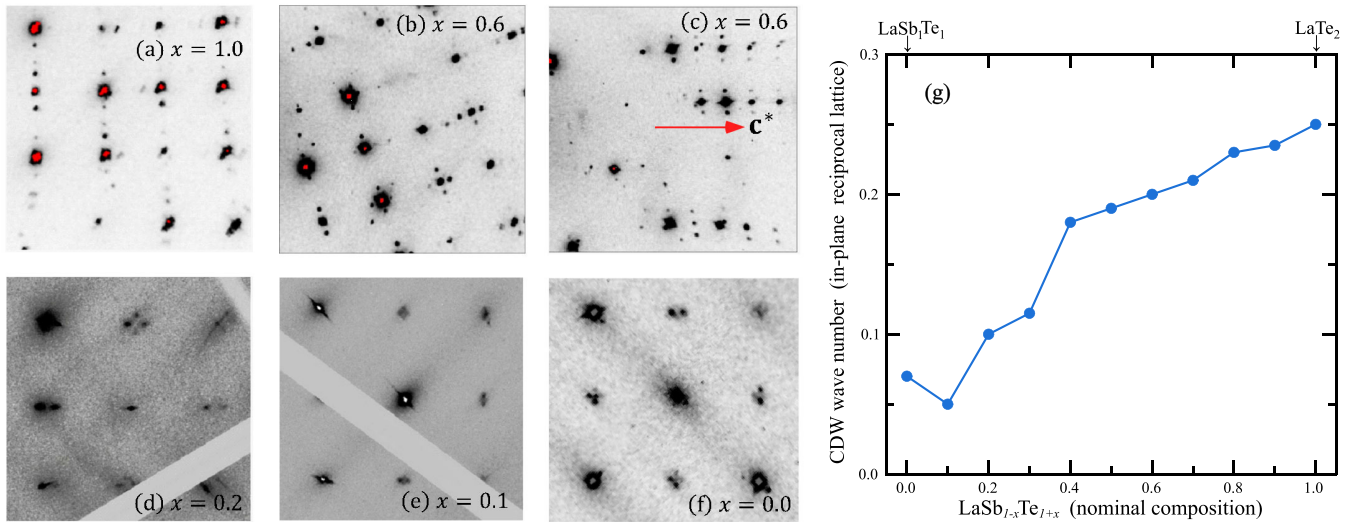
FIG. 2. CCD images of $LaSb_{1-x}Te_{1+x}$ samples with various preparation compositions, acquired during single-crystal structure analyses at room temperature, and (g) the dependence of the charge-density-wave (CDW) wave vector of 1c-structured LaSbTe on the nominal composition. The composition labeled $LaTe_2$ in the graph corresponds approximately to the actual composition $LaSb_{0.5}Te_{1.5}$ (see text). Images (a), (b), and (d)–(f) were obtained with the incident x-ray beam approximately aligned along the crystallographic c axis (stacking direction), whereas image (c) was taken with the beam oriented approximately along the a or b axis (in-plane direction).

between the magnitude of the CDW wave vector and the Sb concentration, the actual Te composition of the nominal $LaTe_2$ sample is estimated to be approximately $LaSb_{0.5}Te_{1.5}$. Moreover, the lattice parameters are also consistent with those reported for a composition corresponding to Sb concentration $x = 0.5$. Preliminary EDX analysis of the $x = 1.0$ sample further suggests a Te-to-Sb ratio of about 2.6, corresponding to an actual composition of $LaSb_{0.56}Te_{1.44}$. Taken together, these results indicate that the actual composition of our nominal $LaTe_2$ ($x = 1.0$) sample is close to $LaSb_{0.5}Te_{1.5}$, although precise determination of the composition will require further analysis using, for example, an electron probe microanalyzer (EPMA).

We calculated the electronic structure of $LaSb_{1-x}Te_{1+x}$ in order to obtain its Fermi surface and to investigate possible CDW nesting vectors, i.e., which Fermi surfaces are involved in nesting, in samples near the stoichiometric composition, which have not been reported so far. The calculations were performed using WIEN2k within the framework of the virtual crystal approximation (VCA). The crystal structures employed in the calculations excluded superlattice reflections and assumed a tetragonal lattice corresponding to the parent structure prior to the CDW transition. Figure 3 expresses the calculated Fermi surfaces on the $k_z = 0$ plane for $LaSb_1Te_1$ ($x = 0$), $LaSb_{0.75}Te_{1.25}$ ($x = 0.25$), $LaSb_{0.5}Te_{1.5}$ ($x = 0.5$), and $LaTe_2$ ($x = 1.0$). The Fermi surfaces at $x = 0.25$, 0.5, and 1.0 are shown for comparison. The calculated results of their electronic structures are provided in Ref. [91]. The obtained results are basically consistent with the previous study [92]. Note that at $x = 0$ the circlelike Fermi surface at the center does not actually exist as suggested by the ARPES study of LaSbTe [57]. The blue arrows shown in the $x = 0.25$, 0.5, and 1.0 panels represent nesting vectors consistent with those observed experimentally by E. DiMasi *et al.*[84]. By analogy

with the cases of $x > 0$ and the observed short wave vector ($\leqslant 0.1$), the superlattice spots observed around $LaSb_1Te_1$ ($x = 0$) can be explained by the formation of a CDW with the nesting vector indicated for $x = 0.0$, shown as the red arrow in the figure. However, because of the very short length of this nesting vector and the poor nesting condition, its influence on the electronic structure—and thus on the electrical properties—should be considered negligible.

Figure 4 shows the temperature dependence of the in-plane resistivity of 1c-LaSbTe as a function of nominal composition. All samples exhibit insulating behavior, which becomes more pronounced with increasing Te concentration. A similar trend has been reported in the Te-rich region of $GdSb_{1-x}Te_{1+x}$, where it is accompanied by a CDW [81]. As shown in Fig. 3, comparison of the Fermi surface nesting among $LaSb_1Te_1$ ($x = 0$)—excluding the central Fermi surfaces noted above— $LaSb_{0.75}Te_{1.25}$ ($x = 0.25$), and $LaSb_{0.5}Te_{1.5}$ ($x = 0.5$) reveals that nesting in $LaSb_{1-x}Te_{1+x}$ with larger x is considerably more complete, as pairs of Fermi surfaces are more nearly parallel. Consequently, in $LaSb_{1-x}Te_{1+x}$ with larger x, most of the Fermi surface is expected to be gapped out by nesting, whereas only partial nesting occurs in $LaSb_1Te_1$ ($x = 0$). This difference in nesting efficiency provides a plausible explanation for the composition-dependent resistivity behavior, i.e., the evolution of the temperature dependence of resistivity, observed in 1c-LaSbTe.

The results presented in this section demonstrate that precise control of band filling has been achieved in the Te-rich region of $LaSb_{1-x}Te_{1+x}$, as evidenced by the continuous variation of the lattice parameter, CDW wave vector, and temperature-dependent resistivity, although this control is effective only up to approximately $x \approx 0.5$. They also highlight the effectiveness of our sample synthesis method, even though the range of control is limited.
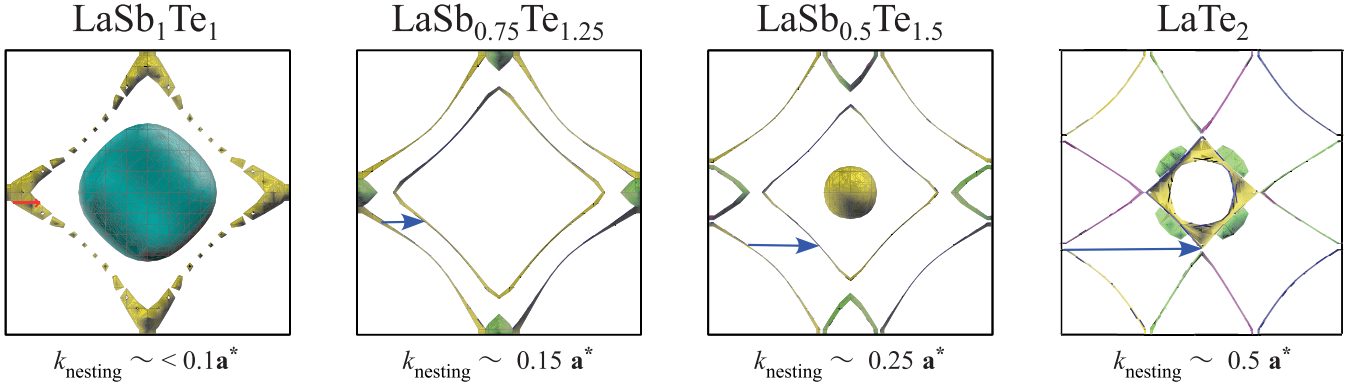
FIG. 3. Calculated Fermi surfaces of $LaSb_{1-x}Te_{1+x}$ at $k_z = 0$ for $x = 0$ ($LaSb_1Te_1$), 0.25 ($LaSb_{0.75}Te_{1.25}$), 0.5 ($LaSb_{0.5}Te_{1.5}$), and 1.0 ($LaTe_2$). Different colors represent contributions from different electronic bands. The possible nesting vector for $x = 0$ is indicated by the red arrow, in analogy with the experimentally observed nesting vectors for $x = 0.25$, 0.5, and 1.0 [84], which are shown by the blue arrows.

2. 2c-LaSbTe, orthorhombic form in Sb-rich region

As mentioned in the introduction, samples of 2c-LaSbTe were obtained within the composition range of $LaSb_{1-x}Te_{1+x}$ ($-0.6 \leqslant x < 0$), corresponding to the Sb-rich region on the preparation composition. For $x < -0.6$, other crystalline phases, such as $LaSb_2$, were simultaneously formed as by-products.

We conducted single-crystal structural analyses of 2c-LaSbTe, which adopts the orthorhombic space group $P2_12_12_1$ (No. 19), in contrast to a previous report that identified the space group as $Pmcn$ (No. 62) [84]. The rationale for assigning $P2_12_12_1$ is as follows.

First, prominent superlattice reflections at high h and k values in the (hkl) diffraction patterns indicated atomic displacements within the ab plane. In the 1c-type structure,

constituent atoms occupy high-symmetry Wyckoff positions ($2a$ and $2c$), and such in-plane displacements would lower the symmetry from a tetragonal to an orthorhombic system.

Among the three orthorhombic point groups—222, $mm2$, and mmm—we found 222 to be most consistent with our observations. The mmm group was excluded because it includes mirror planes perpendicular to the a and b axes within the ab plane, which are incompatible with the inferred atomic displacements (excluding 2_1 screw or glide symmetry associated with unit cell doubling along the c axis). Likewise, $mm2$ was excluded due to the inconsistency of its diagonal glide plane symmetry with the observed diffraction features (again, with the exception of 2_1 screw or glide operation).

Taking these considerations into account, we narrowed the candidate space groups to those belonging to the 222 point group, as well as selected space groups from the mmm and $mm2$ point groups. Among these, we concluded that $P2_12_12_1$ (No. 19) is the most appropriate space group for 2c-structured LaSbTe. Although $Pmcn$ (No. 62), as proposed by DiMasi *et al.*, initially appeared to be a convincing candidate, the calculated diffraction intensities for this space group did not adequately reproduce the experimental data. We therefore examined its subgroup symmetries and found that the non-centrosymmetric space group $P2_12_12_1$ provided a significantly improved fit to the observed reflection intensities. In these structural analyses of 2c-LaSbTe, we confirmed that the R values obtained with $P2_12_12_1$ were systematically lower than those with $Pmcn$. For example, at $x = -0.2$, we obtained $R = 0.0293$ for $P2_12_12_1$ compared with $R = 0.1196$ for $Pmcn$. Additional results for other x values are provided in Ref. [91].

Ultimately, the single crystal of 2c-LaSbTe was found to consist of four structural domains. Specifically, it comprises two primary domains sharing a common c axis but rotated by 90° with respect to each other in the ab plane—a configuration consistent with a transformation from tetragonal to orthorhombic form. Each primary domain is further split into two subdomains with distinct orientations, a phenomenon attributed to the absence of inversion symmetry in the $P2_12_12_1$ space group. In this context, $Pmcn$ can be regarded as the space group representing the averaged structure.
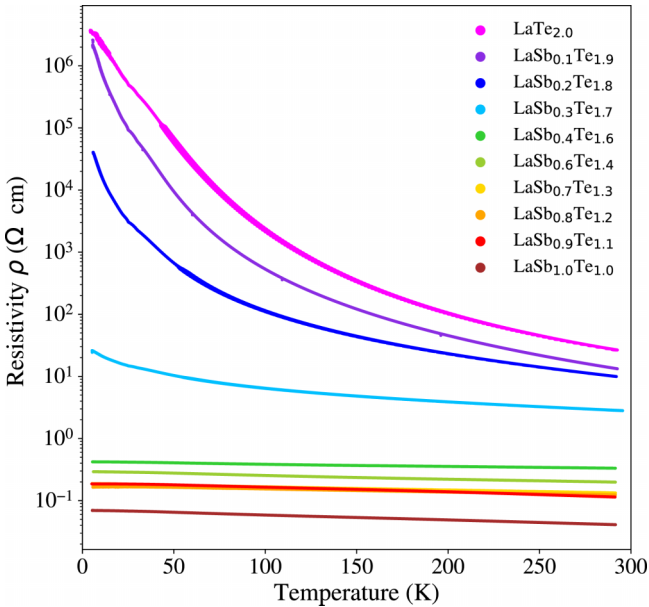

FIG. 4. Temperature dependence of the in-plane resistivity for 1c-structured LaSbTe as a function of nominal composition. The data point labeled $LaTe_2$ corresponds approximately to the actual composition $LaSb_{0.5}Te_{1.5}$ (see text).
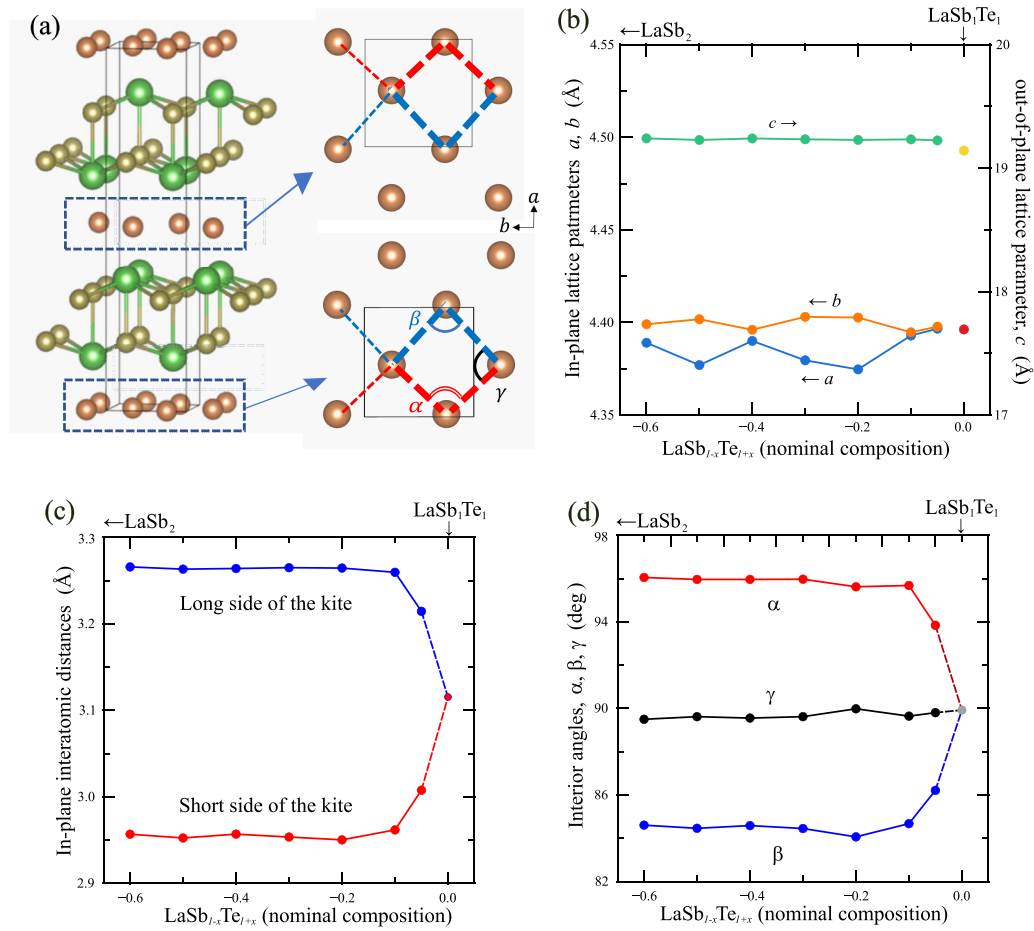
FIG. 5. Crystal structure of 2c-structured LaSbTe (left) and the Sb square nets (right) (a), dependence of the lattice parameters (b), kite lattice lengths (c), and kite lattice angles (d) on the nominal composition. In the right panel of (a), the long and short sides of the kite-shaped lattice are indicated by blue and red dashed lines, respectively.

We conducted crystal structure analyses on a series of LaSb$_{1-x}$Te$_{1+x}$ samples with compositions in the range $-0.6 \leqslant x < 0$, treating all samples nominally as LaSb$_1$Te$_1$. Because Sb and Te are adjacent elements in the lower part of the periodic table, we assumed that their atomic differences would have a negligible effect on the results. This approximation was also employed previously in the structural analyses of Te-rich 1c-LaSbTe, whose results were used in the Fermi surface calculations for 1c-LaSbTe shown in Fig. 3. All single-crystal XRD data for the 2c-structured LaSb$_{1-x}$Te$_{1+x}$ samples ($-0.6 \leqslant x < 0$) were successfully refined, yielding sufficiently low R values, as shown in Ref. [91]. A complete refinement detail for the $x = -0.2$ sample (LaSb$_{1.2}$Te$_{0.8}$), which was used in the subsequent electronic structure calculations, is also provided in Ref. [91].

Figure 5(a) illustrates the crystal structure of the 2c-structured LaSbTe. The structure comprises two primary components: [La–Te] slabs and Sb square lattice sheets. Notably, significant structural modifications are observed in the Sb square lattice sheets. In the 2c-type structure, two such square lattice sheets are present per unit cell, each originally forming a square lattice that is distorted into a kite-shaped configuration. Furthermore, the orientations of the kite-shaped lattices in the two layers are reversed relative to one another, giving rise to a doubling of the periodicity along the stacking c

axis. In contrast, the [La–Te] slabs remain largely unchanged from those in the 1c-type structure, with variations in bond lengths limited to within ± 0.01 Å. A similar distortion from a perfect square to a kite-shaped lattice has also been reported in other square lattice materials [93].

Figures 5(b), 5(c), and 5(d) present the dependence of structural properties—namely, lattice parameters and the shape of the Sb square lattice—on the nominal composition. Figure 5(b) shows the variation of lattice parameters including data for 1c-structured LaSb$_1$Te$_1$ for comparison. The lattice parameters of 2c-LaSbTe remain nearly constant, exhibiting minimal dependence on the preparation composition within the investigated range. The in-plane lattice parameters of the 2c-type structure are nearly identical to those of the 1c-type structure, while the stacking axis in the 2c-type structure is slightly longer than twice the length of the 1c-type structure by approximately 0.08 Å. This elongation is primarily attributed to the displacement of Sb atoms from the symmetry plane, amounting to approximately ± 0.022 Å.

Figures 5(c) and 5(d) illustrate the evolution of the distorted square lattice in 2c-LaSbTe as a function of preparation composition, with the corresponding regions indicated in Fig. 5(a). The results show that the square lattice undergoes a rapid distortion into a kitelike shape when $x > -0.2$, while it largely retains its original configuration for $x \leqslant -0.2$,
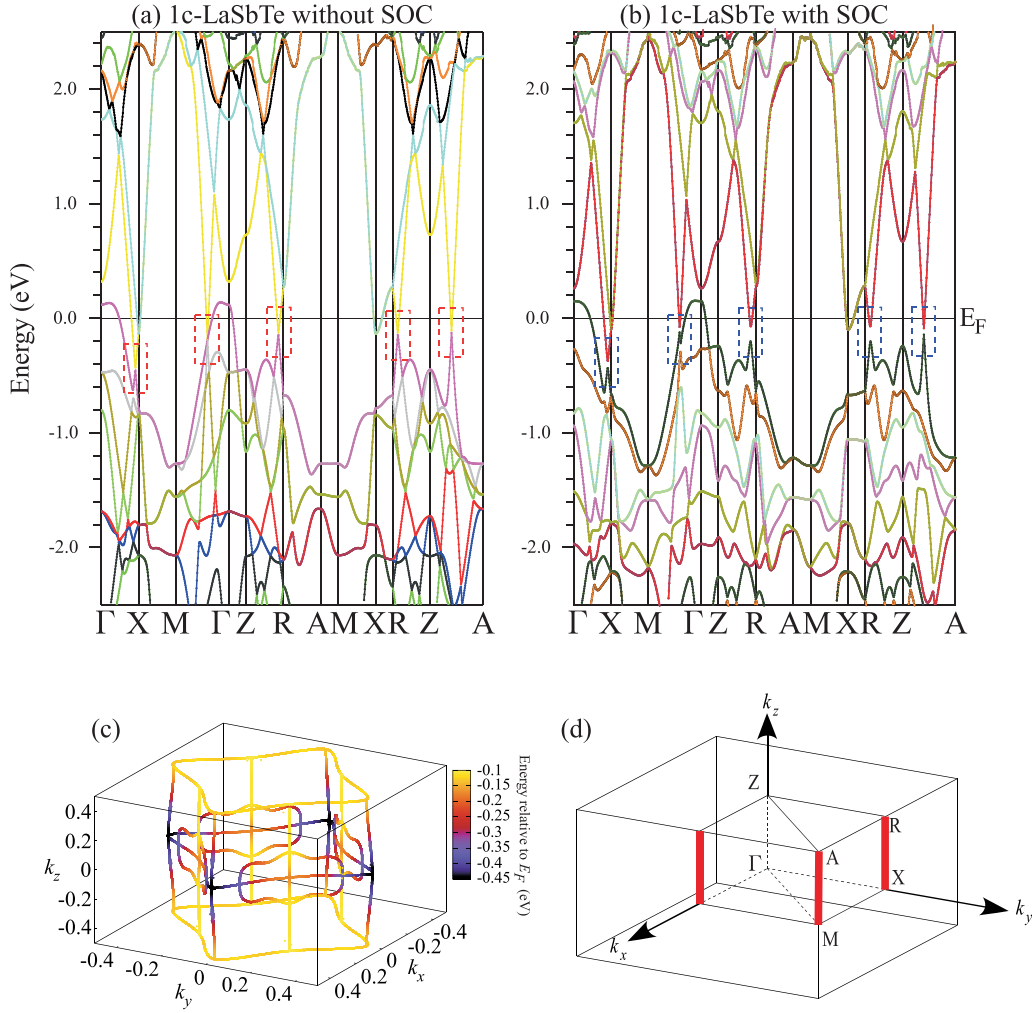
FIG. 6. Electronic band structures of 1c-structured LaSbTe without spin-orbit coupling (SOC) (a) and with SOC (b), band crossings in the first Brillouin zone without SOC (c), and symmetry labels of high-symmetry points (d). In (c), the color scale indicates the energy relative to the Fermi level. Thick red lines in (d) highlight band degeneracies that persist even in the presence of SOC.

with a length variation of approximately $\pm 5\%$. This trend is consistent with previous observations [94]. Additionally, preliminary EDX measurements suggest that the Te composition decreases with preparation composition when $x > -0.3$, while for $x \leqslant -0.3$, the change in composition is markedly suppressed. This observation aligns well with the structural changes presented above.

Next, we focus on the electronic structure of the 2c-structured LaSbTe. The crystal structure of the 2c phase belongs to the orthorhombic space group $P2_12_12_1$, which can be regarded as a subgroup of the tetragonal $P4/nmm$ structure characteristic of the 1c phase. To clarify the distinguishing features of the 2c phase, it is essential to first examine the electronic structure of the 1c phase. Accordingly, we begin by analyzing the relationship between the electronic structure of the 1c phase and its crystallographic symmetry operations.

Previous studies of 1c-structured LaSbTe and ZrSiS family have extensively reported on the topological band crossings in materials with the nonsymmorphic space group $P4/nmm$ [32,57,95–97]. According to these studies, the band crossings are protected by the following crystal symmetry operations: the glide mirror $\tilde{\mathcal{M}}_z = \{\mathcal{M}_z | \frac{1}{2}\frac{1}{2}0\}$, the mirror $\tilde{\mathcal{M}}_x =$

$\{\mathcal{M}_x | \frac{1}{2}00\}$, $\tilde{\mathcal{M}}_y = \{\mathcal{M}_y | 0\frac{1}{2}0\}$, $\tilde{\mathcal{M}}_{xy} = \{\mathcal{M}_{xy} | \frac{1}{2}\frac{1}{2}0\}$, the two screw symmetries, $\tilde{\mathcal{C}}_{2x} = \{\mathcal{C}_{2x} | \frac{1}{2}00\}$ and $\tilde{\mathcal{C}}_{2y} = \{\mathcal{C}_{2y} | 0\frac{1}{2}0\}$ and the spatial inversion $\mathcal{P}$ symmetries. The combination of these symmetries with time-reversal symmetry $\mathcal{T}$ enforces nonsymmorphic degeneracies at the BZ boundary and enables the occurrence of multiple nodal lines inside the BZ.

In the absence of SOC, the combination of screw axis operations, $\tilde{\mathcal{C}}_{2x}$ and $\tilde{\mathcal{C}}_{2y}$, with $\mathcal{T}$ enforces double degenerate states in the M-X-A-R plane at the boundary of the BZ. This characteristic is evident compared of the path along the R-A-M-X-R with other paths in Fig. 6(a), which shows the electronic band structure of 1c-LaSbTe without SOC, calculated based on the result of our crystal structure analysis of LaSb$_1$Te$_1$. In the presence of SOC, most of these degeneracies are lifted, except along the A-M and X-R paths shown in Fig. 6(d), which remain as fourfold degenerate states, as shown in Fig. 6(b), which displays the corresponding band structure with SOC.

Inside the BZ, mirror symmetry operations allow band crossings in planes without SOC; $\tilde{M}_z$ can protect band crossings in the $k_z = 0$ and π planes, $\tilde{M}_x(= \tilde{\mathcal{C}}_{2x}\mathcal{I})$, $\tilde{M}_y(= \tilde{\mathcal{C}}_{2y}\mathcal{I})$, and $\tilde{M}_{xy}$, allow band crossings in the $k_y = 0$ and $k_x = 0$ planes
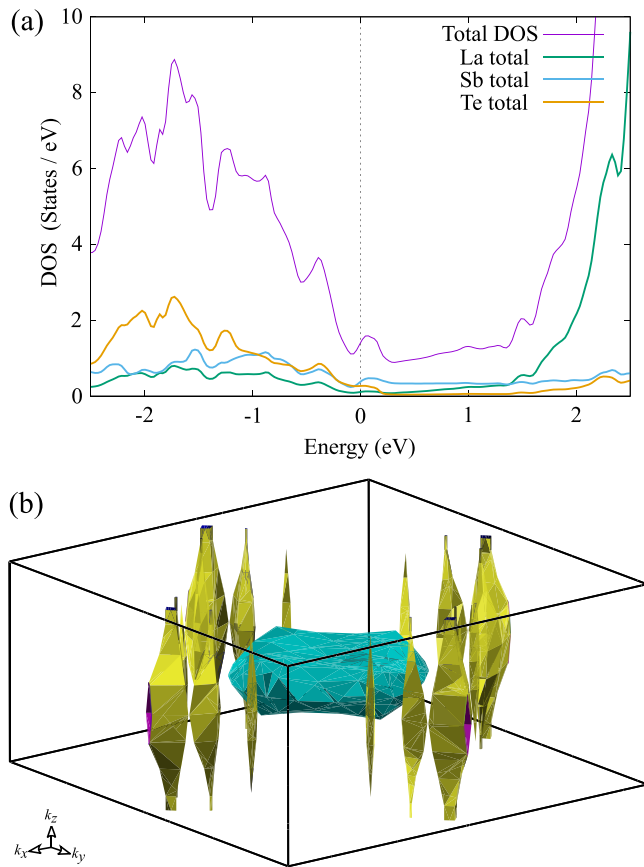
FIG. 7. Density of states (DOS) near the Fermi level (a) and Fermi surfaces (b) of 1c-structured LaSbTe with spin-orbit coupling (SOC). In (b), different colors indicate contributions from different electronic bands.

and the plane given by $k_x = k_y$, respectively. To clarify the allowed band crossings, we calculated them close to the Fermi level inside the BZ.

Figures 6(c) and 6(d) schematically illustrate the calculated band crossings, i.e., the nodal-line configurations, in the absence of SOC and the symmetry labels for high-symmetry points, respectively. The nodal loops in the $k_z = 0$ and π planes are interconnected by three additional nodal lines extending along the k_z direction, which are protected by $\tilde{\mathcal{M}}_x$ and $\tilde{\mathcal{M}}_{xy}$. These nodal loops and interconnecting lines are also indicated by the red rectangular boxes in Fig. 6(a). They are completely consistent with the previously-reported results [57,96].

These nodal lines within the BZ are twofold degenerate in the absence of SOC, but they become unstable and are lifted upon the inclusion of SOC, resulting in the opening of narrow energy gaps. As shown in the comparison between Fig. 6(a) and 6(b), the band crossings in (a) are lifted and form narrow gaps indicated by the blue boxes in (b) in the presence of SOC. Consequently, only the degeneracies at the BZ boundary remain, as highlighted by the thick red lines in Fig. 6(d).

Figure 7(a) shows the calculated density of states (DOS) near the Fermi level for the 1c-type structure with SOC. The Fermi level lies at the bottom of a low-DOS region, which primarily originates from the upper part of the parabolic band

associated with the Sb conducting layer. Consequently, in the Te-rich region, the Fermi surface is dominated by this simple parabolic band, featuring a large quasi-one-dimensional portion that favors nesting and thereby drives a CDW transition on the tetragonal lattice. By contrast, states just below the Fermi level derive from both the lower part of the Sb parabolic band and the electronic states of the [La–Te] slab. In the Sb-rich region, the resulting Fermi surfaces are thus expected to be more complex and less favorable for nesting. Instead, a different type of lattice distortion lifts the high symmetry of the 1c phase, giving rise to the 2c phase.

Figure 7(b) shows the calculated Fermi surfaces of 1c-LaSbTe with SOC. Note that the band giving the circlelike Fermi surface centered at Γ was suggested by the ARPES study of LaSbTe to lie below the Fermi level [57]. The other Fermi surfaces around X are derived from the upper band forming the band crossings shown in Fig. 6(c), because the Fermi level of 1c-LaSbTe is located slightly above the nodal-line crossings.

We now turn to the discussion of the electronic structure of 2c-LaSbTe. Figures 8(a) and 8(b) present the calculated band structures without and with SOC, respectively. The corresponding enlarged views in the $k_z = 0$ plane are provided in Ref. [91]. The actual Fermi level in 2c-LaSbTe is expected to lie below that shown here, because the calculations were based on the crystal structure determined for LaSb$_{1.2}$Te$_{0.8}$, while assuming the composition LaSb$_1$Te$_1$. As shown in both panels, pronounced anisotropy is evident along the k_x and k_y directions. This arises from the distortion of the Sb square lattice into a kitelike configuration. The electronic states near X remain at the Fermi level, whereas those near Y are suppressed.

The nonsymmorphic symmetry $P2_12_12_1$ for 2c-LaSbTe has the three screw symmetries, $\tilde{\mathcal{C}}'_{2x} = \{\mathcal{C}_{2x}|\frac{1}{2}\frac{1}{2}0\}$, $\tilde{\mathcal{C}}'_{2y} = \{\mathcal{C}_{2y}|0\frac{1}{2}\frac{1}{2}\}$, $\tilde{\mathcal{C}}'_{2z} = \{\mathcal{C}_{2z}|\frac{1}{2}0\frac{1}{2}\}$, the combination of these screw axis operations with $\tilde{\mathcal{T}}$ enforces double degenerate states at the boundary of the BZ in the absence of SOC. These degeneracies can be observed in Fig. 8(a), particularly along the X-S-Y and S-R-Z-T-R-U-Z paths. Upon introducing SOC, most of these degeneracies are lifted, except at the high-symmetry points U, T, and S, where they remain protected by the space group symmetry and $\mathcal{T}$, as shown in Fig. 8(b).

Furthermore, two important observations can be made.

(1) A comparison of the number of electronic bands between the calculations with and without SOC, as shown in Figs. 8(a) and 8(b), along a nondegenerate path (such as Γ–X), reveals that the degree of inversion-symmetry breaking is negligible, as the same number of band lines appear in both cases. In fact, the difference in the virtual center positions defined by the La–Te slab and the Sb layers, which coincide completely with each other in the original 1c-type structure, is only about 0.011 in relative fractional coordinates within the ab plane of the unit cell, indicating an extremely small structural asymmetry.

(2) The comparison of the electronic band structures without SOC along the T-R line with those along other segments of the S-R-Z-T-R-U-Z path, as shown in Fig. 8(a), suggests the presence of a hidden symmetry operation beyond the intrinsic symmetries of the $P2_12_12_1$ space group. This inference arises from the apparent degeneracies observed along
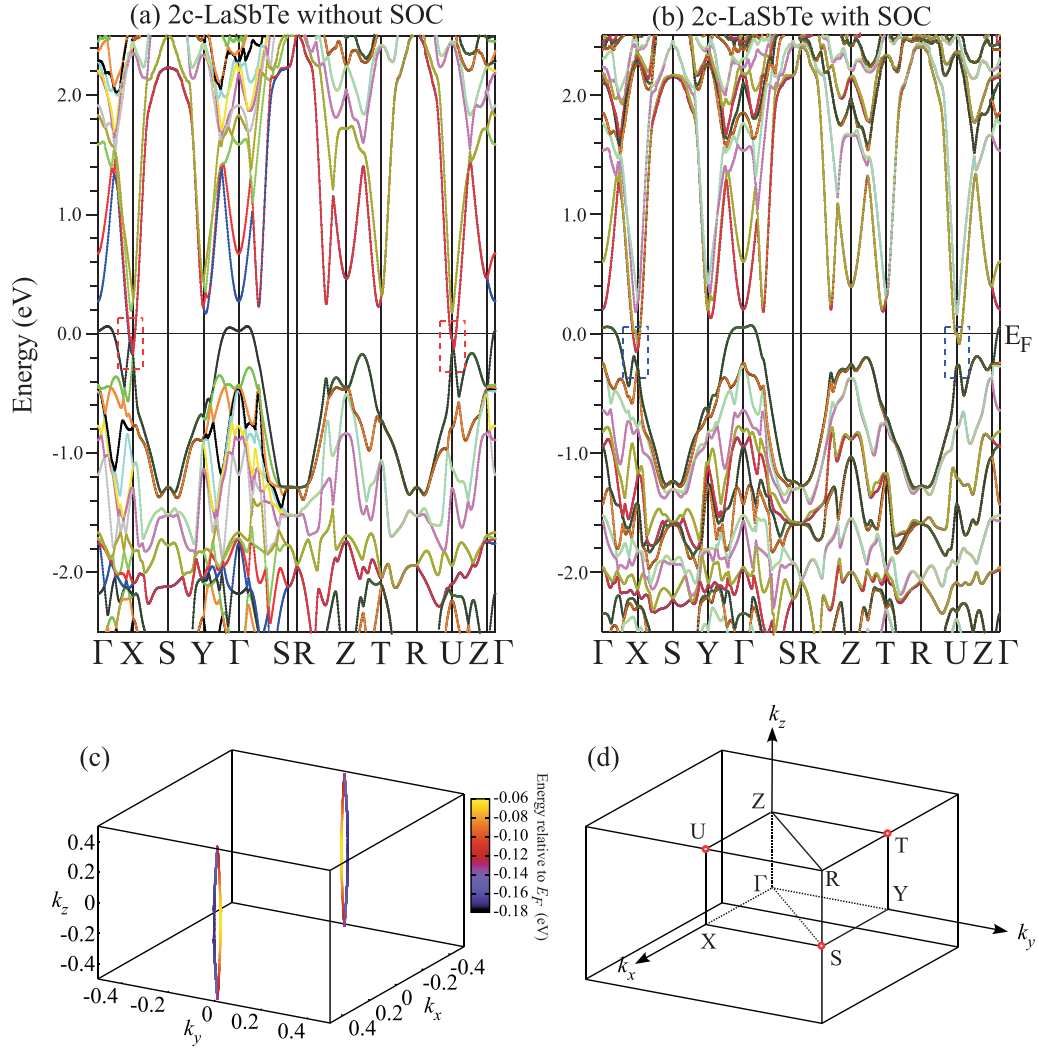
FIG. 8. Electronic band structures of 2c-structured LaSbTe (LaSb$_{1.2}$Te$_{0.8}$) without spin-orbit coupling (SOC) (a) and with SOC (b), band crossings in the first Brillouin zone without SOC (c), and symmetry labels of high-symmetry points (d). In (c), the color scale indicates the energy relative to the Fermi level. Thick red points in (d) highlight band degeneracies that persist even in the presence of SOC. These results are based on the crystal structure of LaSb$_{1.2}$Te$_{0.8}$ and the assumed composition LaSb$_1$Te$_1$; therefore, the actual Fermi level in (a) and (b) is expected to lie below the value shown (see text).

the T-R line, as such degeneracies are typically associated with specific symmetry operations. We attribute this hidden symmetry to $\tilde{\mathcal{M}}_y$ in the original cell, which belongs to the $P4/nmm$ space group. The key structural difference between the 1c and 2c phases lies in the kite-shaped lattice distortion, which evidently breaks $\tilde{\mathcal{M}}_x$ and $\tilde{\mathcal{M}}_{xy}$, while preserving $\tilde{\mathcal{M}}_y$.

Figures 8(c) and 8(d) present a schematic representation of the calculated band crossing configurations near the Fermi level in the BZ for the 2c-type structure without SOC and the symmetry labels of the high-symmetry points. Compared to Fig. 6(c), only the band crossings protected by the glide mirror symmetry $\tilde{\mathcal{M}}_y$ remain. These are folded along the k_z direction due to the doubled periodicity along the c axis. The corresponding crossings are indicated by the red rectangular boxes in Fig. 8(a). As in the 1c-type structure, these nodal lines are twofold degenerate in the absence of SOC but are gapped out when SOC is introduced, as shown in the blue rectangular boxes in Fig. 8(b). Consequently, only the degeneracies at the

BZ boundary persist, which are highlighted by the thick red circles in Fig. 8(d).

Figure 9(a) presents the calculated DOS for the 2c-type structure with SOC near the Fermi level. In contrast to the 1c-type structure shown in Fig. 7(a), the DOS around the Fermi level is markedly reduced, exhibiting a pronounced dip. A detailed comparison with the DOS of 1c-LaSbTe reveals that this significant reduction primarily originates from the Sb atoms, which form a kite-shaped lattice configuration within the Sb conducting layer, as the contribution from Sb atoms (Sb total) changes substantially compared with those of the other constituent atoms. These findings strongly suggest that the lattice deformation is predominantly driven by electronic energy gain, specifically through the band Jahn-Teller effect, as previously proposed in the literature [98].

Figure 9(b) shows the calculated Fermi surfaces of 2c-structured LaSbTe with SOC. The Fermi surfaces around X originate from the upper band that forms the band crossing
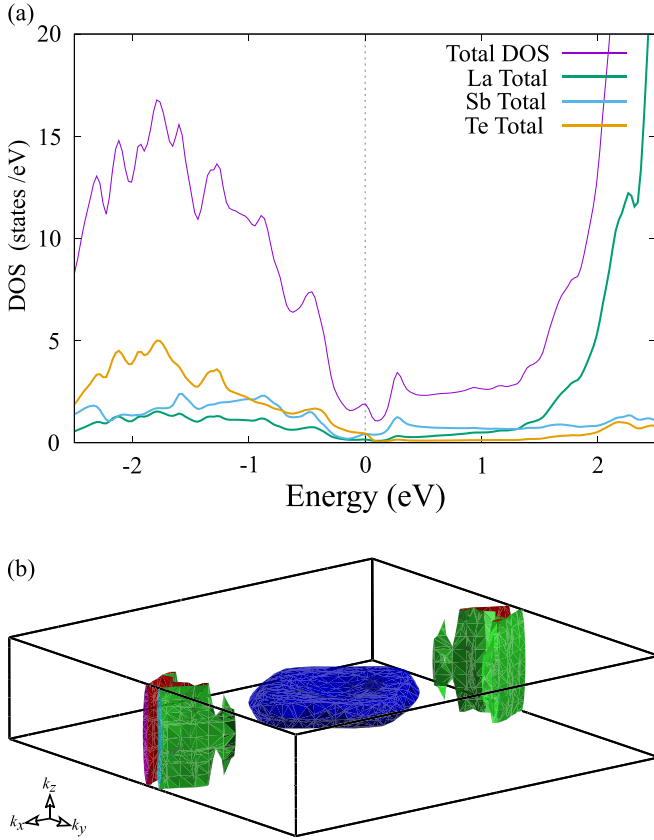
(a)

(b)

FIG. 9. Density of states (DOS) near the Fermi level (a) and Fermi surfaces (b) of 2c-structured LaSbTe with spin-orbit coupling (SOC). In (b), different colors indicate contributions from different electronic bands. These results are based on the crystal structure of $LaSb_{1.2}Te_{0.8}$ and the assumed composition $LaSb_1Te_1$, and should therefore be interpreted with caution (see text).

shown in Fig. 8(c). This result should be interpreted with caution, as it was obtained from calculations based on the crystal structure of $LaSb_{1.2}Te_{0.8}$ and the assumed composition $LaSb_1Te_1$, as mentioned above; the actual Fermi surface is expected to deviate slightly owing to a downward shift of the Fermi level. Nevertheless, the overall Fermi surface closely resembles that reported in previous ARPES measurements [94], apart from the lumplike feature centered at Γ. As in the case of the 1c-type structure, this feature should be considered to lie below the Fermi level.

Figure 10 shows the temperature dependence of the in-plane resistivity of 2c-structured LaSbTe as a function of preparation composition. Although the absolute resistivity values vary within a narrow range, the overall temperature dependence changes gradually. The insulating character weakens as the composition shifts from $LaSb_1Te_1$, eventually giving way to metallic behavior in $LaSb_{1.4}Te_{0.6}$. As noted above, in the range $x = -0.05$ to -0.3, the electronic structure gradually evolves from that of 1c-LaSbTe to that of 2c-LaSbTe: the gap opens at X, the states around Y diminish, and the Fermi level simultaneously shifts downwards as the Sb content increases. Therefore, a more detailed investigation of the relationship between the electronic structure and the electrical properties is an important task for future research
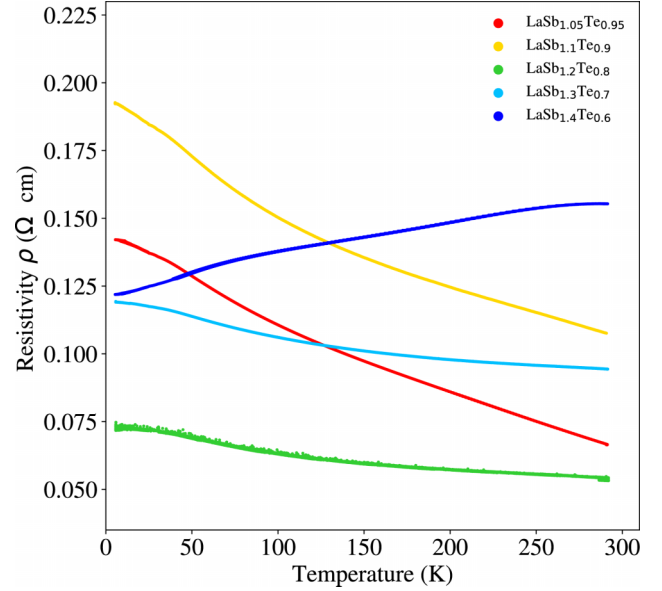

FIG. 10. Temperature dependence of the in-plane resistivity for 2c-structured LaSbTe as a function of nominal composition.

on 2c-structured LaSbTe in this composition range. At lower x, according to the rigid-band model, the Fermi level of 2c-LaSbTe resides in a dip in the DOS, as shown in Fig. 9(a). Further lowering of the Fermi level with increasing Sb content leads to a higher DOS, i.e., metallic behavior, which qualitatively accounts for the observed composition-dependent resistivity variations.

In this section, we have presented the structural and electronic properties of 2c-structured LaSbTe, in which the conducting Sb square lattice is distorted into a kite-shaped configuration. This distortion induces significant modifications in the electronic structure: most states near the Fermi level are suppressed, leaving only those associated with band crossings arising from a quasisymmetry operation, $\tilde{\mathcal{M}}_y$ in the original cell. Here, "quasi" indicates that the symmetry operation is preserved locally within the kite-type lattice but not by the overall crystal structure [99]. As a result, a narrow-gap electronic structure emerges in the presence of SOC. Similar to the observations in the Te-rich region, precise tuning of the band filling was achieved in the compositional range $-0.3 < x < 0$ in $LaSb_{1-x}Te_{1+x}$. This is evidenced by the continuous variation in the distortion of the Sb square lattice, which reflects a systematic modulation of the electronic structure. Taken together with the results obtained in the Te-rich region, these findings indicate that our sample synthesis method is effective near the stoichiometric composition $LaSb_1Te_1$.

B. YSbTe

Yttrium (Y) has one of the smallest atomic radii among the rare-earth elements, enabling the formation of YSbTe as a member of the RSbTe family of materials. This is attributed to the fact that the atomic radius of Y lies between those of holmium (Ho) and dysprosium (Dy), which have been reported as the smallest rare-earth elements capable of forming RSbTe compounds [56]. Furthermore, based on its constituent
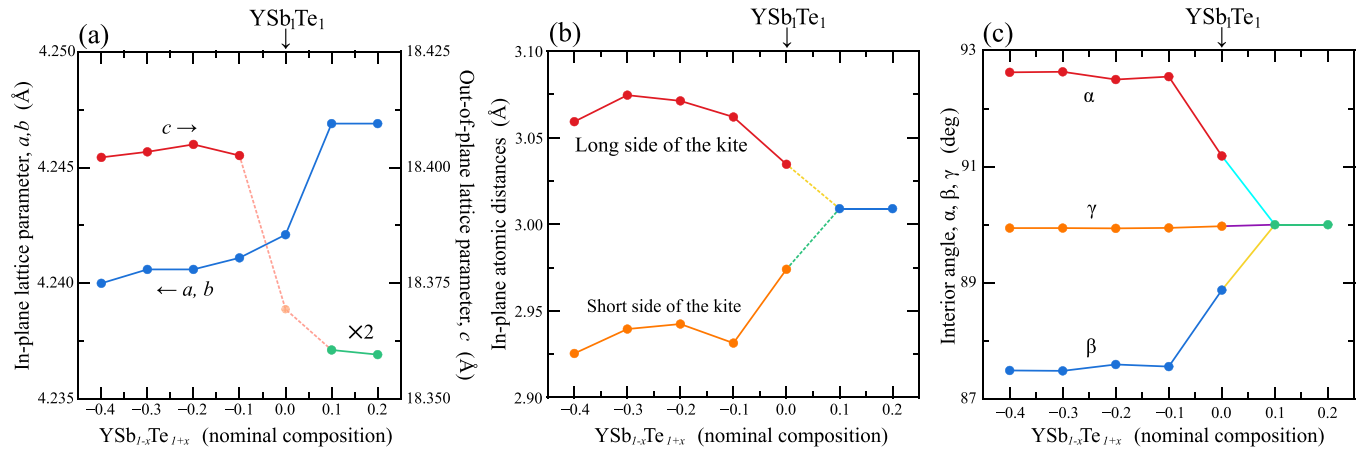
FIG. 11. Dependence of the lattice parameters (a), kite lattice lengths (b), and kite lattice angles (c) of $YSb_{1-x}Te_{1+x}$ on the nominal composition.

elements, YSbTe is considered the compound most closely related to ZrSnTe, a member of the ZrSiS family, because Y and Sb are adjacent to Zr and Sn, respectively, in the periodic table. This elemental proximity offers a unique opportunity to explore differences in the structural and electronic properties between the two material systems.

Single-crystalline samples of YSbTe were prepared in the composition range $YSb_{1-x}Te_{1+x}$ ($-0.4 \leqslant x \leqslant 0.2$). Even for $x > 0.2$, single-crystalline samples were obtained, but they decomposed quickly upon exposure to air. These samples crystallize in a 1c structure in the Te-rich region and a 2c structure in the Sb-rich region, similar to the composition-dependent behavior observed in the LaSbTe system. In the 1c-structure, no superlattice spots indicating the presence of a CDW were observed at room temperature.

We performed crystal structure analyses on a series of $YSb_{1-x}Te_{1+x}$ samples ($-0.4 \leqslant x \leqslant 0.2$), treating all compositions nominally as YSb_1Te_1. As noted in the structural analysis of 2c-LaSbTe, this assumption is not expected to significantly affect the results because Sb and Te are neighboring elements in the lower part of the periodic table. All single-crystal XRD data for $YSb_{1-x}Te_{1+x}$ within this composition range were successfully refined, yielding sufficiently low R values, as shown in Ref. [91]. Complete refinement details for $x = 0.1$, 0.0, and -0.3, which were used for the electronic structure calculations, are also provided in Ref. [91].

It is noteworthy that in the YSbTe series, the composition YSb_1Te_1 ($x = 0$) already exhibits weak 2c superlattice reflections, indicating that this stoichiometry crystallizes in a 2c-type structure. The dependence of lattice parameters on the preparation composition, as shown in Fig. 11(a), indicates that YSb_1Te_1 occupies an intermediate position between 1c- and 2c-structural phases: the in-plane lattice constants, a and b, of YSb_1Te_1 correspond to the 2c structure, while the stacking axis c aligns with the 1c-structure. This result is somewhat understandable, as LaSbSe, which contains smaller Se atoms compared to Te, has been reported to crystallize in a double-stacking structure similar to the 2c structure despite a different space group [100]. These findings indicate that precise single-crystal structure analyses are essential for RSbTe

materials, particularly those incorporating rare-earth elements with atomic radii as small as that of Y.

Figures 11(b) and 11(c) present the dependence of the distorted square lattice on the preparation composition in the $YSb_{1-x}Te_{1+x}$ system over the range $-0.4 \leqslant x \leqslant 0.2$. Notably, the magnitude of the overall lattice distortion in YSbTe ($\approx \pm 2\%$ at $x = -0.3$) is less than half that observed in 2c-LaSbTe ($\approx \pm 5\%$ at $x = -0.2$). This reduced distortion should be attributed to the intrinsically smaller Sb square lattice in YSbTe compared to that in LaSbTe. The suppression of distortion implies enhanced structural rigidity in the Sb square lattice of YSbTe, which likely accounts for the absence of CDW signatures in the Te-rich region.

To investigate the relationship between the weak 2c-type structural distortion and the electronic structure—including its topological features—we performed first-principles electronic structure calculations for YSb_1Te_1 with a lattice distortion of $\leqslant \pm 1\%$. Figures 12(a) and 12(b) show the calculated band structures without and with SOC, respectively. Enlarged views in the $k_z = 0$ plane are provided in Ref. [91]. As indicated by the circles in both panels, an energy gap begins to open around the Y point, which is characteristic of the 2c structure, but it has not yet fully developed, resulting in only subtle modifications of the electronic structure. Indeed, the calculated Fermi surface shown in Fig. 12(d) and the DOS provided in Ref. [91] do not exhibit the clear signatures of the 2c-type structure observed in 2c-LaSbTe; rather, they resemble those of 1c-LaSbTe.

However, the topological features of the electronic structure differ significantly. Figure 12(c) presents a schematic of the calculated zero-gap configurations within the BZ near the Fermi level for weakly 2c-structured YSb_1Te_1 in the absence of SOC. Similar to the case of 2c-structured LaSbTe, the band crossings permitted by the quasi-$\tilde{\mathcal{M}}_y$ symmetry operation are preserved and folded along the k_z direction. This result clearly demonstrates that, although the electronic band structure appears only marginally altered at first glance—reflecting the slight distortion of the square lattice—even minor symmetry breaking can lift most of the nodal-line band crossings within the BZ. As in 2c-LaSbTe,
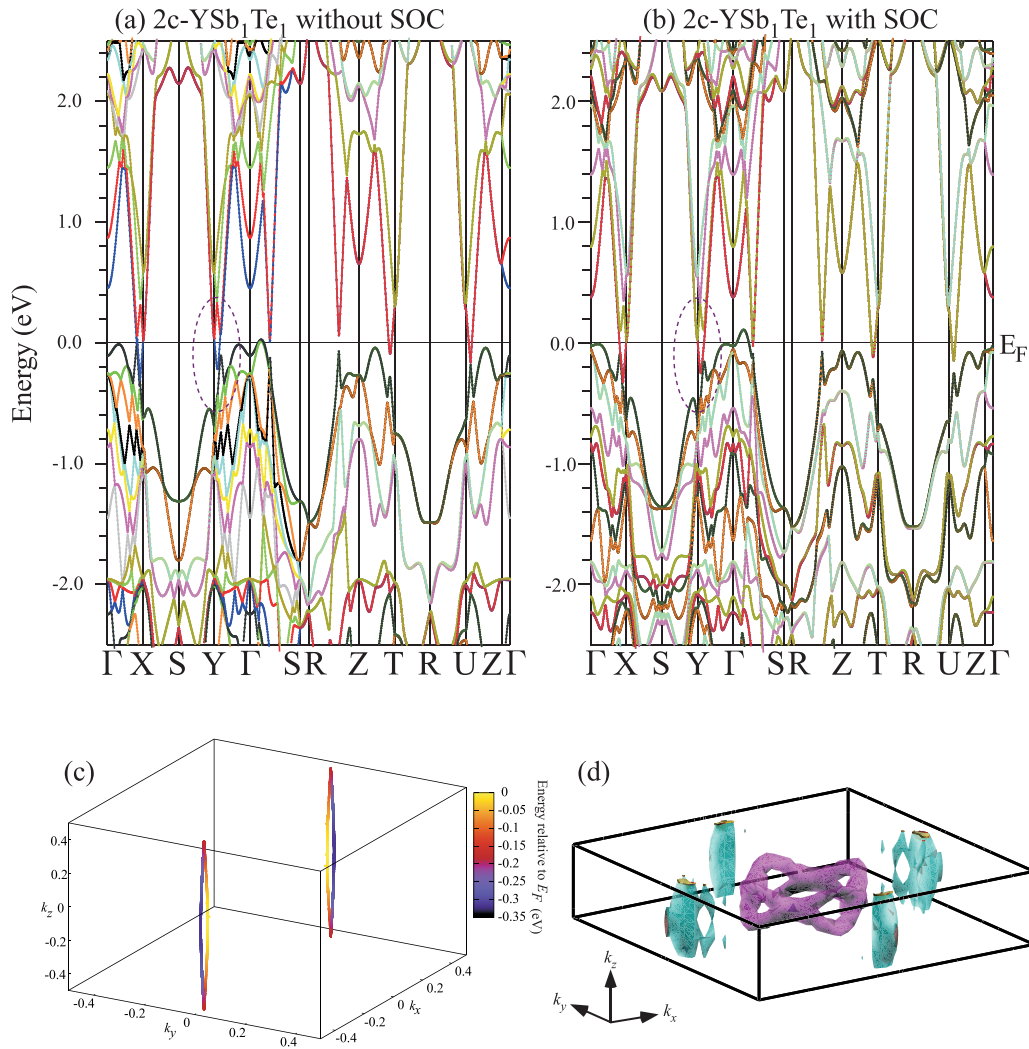
FIG. 12. Electronic band structures of 2c-structured YSb_1Te_1 without spin-orbit coupling (SOC) (a) and with SOC (b), band crossings within the first Brillouin zone without SOC (c) and Fermi surfaces with SOC (d). In (c), the color scale indicates the energy relative to the Fermi level. In (d), different colors indicate contributions from different electronic bands.

the remaining nodal lines are twofold degenerate and are gapped out in the presence of SOC.

To more clearly elucidate the electronic structure characteristics associated with the 2c phase in the YSbTe system, we further investigated $YSb_{1.3}Te_{0.7}$ under a lattice distortion of $\pm 2\%$, which undergoes a complete structural transition into the 2c phase, as inferred from its lattice parameters. Detailed electronic structure analyses of $YSb_{1.3}Te_{0.7}$ are presented in Ref. [91]. The corresponding modifications in the electronic structure—particularly the magnitude of the band gap opening near the Y point—were evident, albeit less pronounced than those observed in the 2c phase of LaSbTe. For instance, the energy gap near the Y point is approximately 0.15 eV in $YSb_{1.3}Te_{0.7}$, in contrast to a significantly larger gap of 0.8 eV in $LaSb_{1.2}Te_{0.8}$, as shown in Fig. 8(b). This discrepancy reflects the relatively minor distortion of the Sb square lattice in the YSbTe system.

Figure 13 illustrates the temperature dependence of the in-plane resistivity for $YSb_{1-x}Te_{1+x}$ ($x = -0.2, -0.1, 0.0, 0.2$), based on the preparation composition. The overall temperature dependence follows a trend similar to that observed in LaSbTe. In the Te-rich region, where samples crystallize in the 1c-type structure, $YSb_{0.8}Te_{1.2}$ exhibits weakly insulating behavior, comparable to that of $LaSb_{1-x}Te_{1+x}$ around $x = 0.0$ (e.g., $R_{10\,K}/R_{300\,K} = 0.07/0.04$ at $x = 0.0$), where a short wave vector CDW has been observed. This behavior is indicative of a semimetallic electronic nature.

In contrast, in the Sb-rich region, $YSb_{1.2}Te_{0.8}$ exhibits metallic behavior, resembling that of $LaSb_{1.4}Te_{0.6}$ in the same compositional regime. This metallicity is consistent with the enhanced DOS at the Fermi level, as previously discussed in the case of 2c-LaSbTe.

In the intermediate composition range, where the square lattice undergoes gradual distortion, no clear insulating behavior is observed–unlike in $LaSb_{1-x}Te_{1+x}$ ($-0.2 \leqslant x \leqslant 0$), which exhibits distinct weakly insulating characteristics. This difference can be attributed to the smaller degree of lattice distortion compared with that in 2c-LaSbTe, leading to only minor modifications of the Fermi surfaces, as shown in Fig. 12(d).
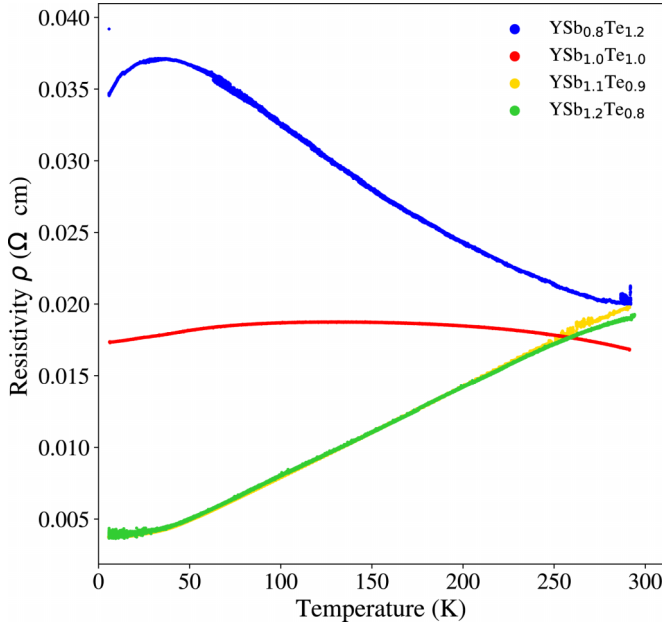
FIG. 13. Temperature dependence of the in-plane resistivity for $YSb_{1-x}Te_{1+x}$ as a function of nominal composition.

So far, we have presented the structural and electrical properties of $YSb_{1-x}Te_{1+x}$ over the range $-0.4 \leqslant x \leqslant 0.2$. Similar to the LaSbTe system, the YSbTe system adopts a 1c-type structure in the Te-rich region and a 2c-type structure in the Sb-rich region. Although the distortion of the Sb square lattice in YSbTe is significantly smaller than that in LaSbTe—suggesting only minor changes in the electronic structure—the topology of the electronic structure, governed by crystal symmetry, clearly transitions to that of the 2c-type structure, even in stoichiometric YSb_1Te_1, which exhibits a lattice distortion of only $\pm 1\%$.

Lastly, we briefly compare the electronic structures of YSbTe from the RSbTe family and ZrSnTe from the ZrSiS family, using structural data for 1c-structured $YSb_{0.9}Te_{1.1}$. Detailed calculation results of electronic structures, Fermi surfaces, and zero-gap configurations for $YSb_{0.9}Te_{1.1}$ and ZrSnTe are provided in Ref. [91].

Although the constituent elements of YSbTe and ZrSnTe are adjacent in the periodic table, their electronic structures belong to distinct systems. As a result, significant differences arise in the configuration of the band crossings within the BZ and in the Fermi surfaces. These differences stem from variations in the atomic orbitals that contribute to the electronic states near the Fermi level.

Figure 14 presents the DOS for $YSb_{0.9}Te_{1.1}$ (a) and ZrSnTe (b). In YSbTe, the electronic states near the Fermi level primarily originate from Te and Sb, with Te and Sb making significantly larger contributions than Y (Te $\approx$ Sb $\gg$ Y). In contrast, for ZrSnTe, the dominant contribution comes from Zr, while Sn and Te play relatively smaller roles (Zr $\gg$ Sn $\approx$ Te). These results indicate that the structural model described earlier, in which the crystal consists of an insulating slablike part ([R-Te] and [Zr-Te]) and a conducting layer (Sb and Sn square lattices), applies to YSbTe but not to ZrSnTe.
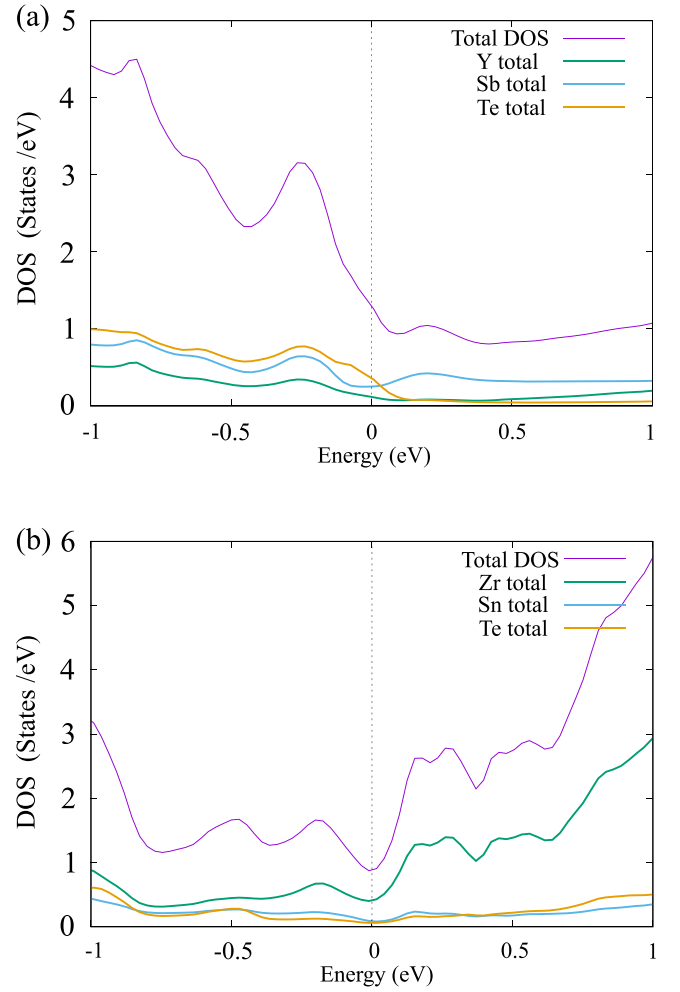

FIG. 14. Comparison of Density of states (DOS) between 1c-structured YSbTe ($YSb_{0.9}Te_{1.1}$) and ZrSnTe.

In summary, the RSbTe system possesses a well-defined layered crystal structure and exhibits low-dimensional electronic characteristics, which can give rise to CDW instabilities, as observed in LaSbTe. This stands in contrast to the ZrSnTe system and also provides an explanation for the failure of our attempts to control band filling in ZrSnTe using the Sn-flux growth method. Although high-quality single crystals of ZrSnTe were successfully synthesized, no systematic variations in their structural or transport properties were detected, likely due to the ineffectiveness of atomic substitution. These results highlight that the RSbTe system is more promising than the ZrSiS family for investigating topological properties through Fermi level tuning and electronic structure modulation.

IV. SUMMARY

We successfully synthesized single-crystalline band filling-controlled samples of $LaSb_{1-x}Te_{1+x}$ and $YSb_{1-x}Te_{1+x}$ and studied their structural and electrical properties. We found that the ratio of R to Te in the preparation process is a key parameter for obtaining band-filling-controlled RSbTe samples using the Sb-flux method. This sensitivity arises from

the difference in electronegativity between Te and Sb atoms, indicating that the preparation composition of the ingredients for synthesizing RSbTe needs to be precise.

In LaSbTe, we found that the Te-rich region stabilizes in a tetragonal structure with a CDW, whereas the Sb-rich region adopts an orthorhombic structure with space group $P2_12_12_1$ (No. 19), characterized by a distorted kite-shaped lattice in the conducting Sb layers. These results can be understood as a symmetry reduction from the high-symmetry $P4/nmm$ (No. 129) structure of LaSbTe, driven either by the CDW transition in the Te-rich region or by a lattice distortion from a square to a kitelike configuration, likely associated with a Jahn-Teller effect, in the Sb-rich region. The electronic structure of the orthorhombic phase with kite-shaped distortion does not evolve into a fully gapped insulator, but rather remains a narrow-gap semiconductor. This behavior arises because a $\tilde{\mathcal{M}}_y$ symmetry operation in the original cell—preserved locally within the kitelike lattice but not by the global crystal structure—protects certain band crossings in the absence of SOC, thereby yielding a narrow gap even when SOC is included.

In YSbTe, we found that the structural properties follow the same trend as observed in LaSbTe, although no CDW was observed in the Te-rich region and the Sb-rich region exhibited less lattice distortion. This is likely due to the smaller, and potentially more rigid, square lattice in YSbTe system.

DATA AVAILABILITY

The data that support the findings of this article are not publicly available. The data are available from the authors upon reasonable request.

---

[1] L. Fu and C. L. Kane, Topological insulators with inversion symmetry, Phys. Rev. B **76**, 045302 (2007).

[2] D. Hsieh, D. Qian, L. Wray, Y. Xia, Y. S. Hor, R. J. Cava, and M. Z. Hasan, A topological Dirac insulator in a quantum spin hall phase, Nature (London) **452**, 970 (2008).

[3] Y. Xia, D. Qian, D. Hsieh, L. Wray, A. Pal, H. Lin, A. Bansil, D. Grauer, Y. S. Hor, R. J. Cava, and M. Z. Hasan, Observation of a large-gap topological-insulator class with a single Dirac cone on the surface, Nat. Phys. **5**, 398 (2009).

[4] H. Zhang, C. X. Liu, X. L. Qi, X. Dai, Z. Fang, and S. C. Zhang, Topological insulators in Bi_2Se_3, Bi_2Te_3 and Sb_2Te_3 with a single Dirac cone on the surface, Nat. Phys. **5**, 438 (2009).

[5] Y. L. Chen, J. G. Analytis, J.-H. Chu, Z. K. Liu, S.-K. Mo, X. L. Qi, H. J. Zhang, D. H. Lu, X. Dai, Z. Fang, S. C. Zhang, I. R. Fisher, Z. Hussain, and Z.-X. Shen, Experimental realization of a three-dimensional topological insulator, Bi_2Te_3, Science **325**, 178 (2009).

[6] J. E. Moore, The birth of topological insulators, Nature (London) **464**, 194 (2010).

[7] M. Z. Hasan and C. L. Kane, Colloquium: Topological insulators, Rev. Mod. Phys. **82**, 3045 (2010).

[8] X.-L. Qi and S.-C. Zhang, Topological insulators and superconductors, Rev. Mod. Phys. **83**, 1057 (2011).

[9] M. Z. Hasan, S.-Y. Xu, and M. Neupane, Topological insulators, topological Dirac semimetals, topological crystalline insulators, and topological Kondo insulators, in *Topological Insulators: Fundamentals and Perspectives*, edited by F. Ortmann *et al.* (John Wiley & Sons, 2015), pp. 55–100.

[10] Y. Ando and L. Fu, Topological crystalline insulators and topological superconductors: From concepts to materials, Annu. Rev. Condens. Matter Phys. **6**, 361 (2015).

[11] M. Sato and Y. Ando, Topological superconductors: A review, Rep. Prog. Phys. **80**, 076501 (2017).

[12] N. P. Armitage, E. J. Mele, and A. Vishwanath, Weyl and Dirac semimetals in three-dimensional solids, Rev. Mod. Phys. **90**, 015001 (2018).

[13] A. Bernevig, H. Weng, Z. Fang, and X. Dai, Recent progress in the study of topological semimetals, J. Phys. Soc. Jpn. **87**, 041001 (2018).

[14] L. Fu, Topological crystalline insulators, Phys. Rev. Lett. **106**, 106802 (2011).

[15] B.-J. Yang and N. Nagaosa, Classification of stable three-dimensional Dirac semimetals with nontrivial topology, Nat. Commun. **5**, 4898 (2014).

[16] S. M. Young and C. L. Kane, Dirac semimetals in two dimensions, Phys. Rev. Lett. **115**, 126803 (2015).

[17] X. G. Wan, A. M. Turner, A. Vishwanath, and S. Y. Savrasov, Topological semimetal and Fermi-arc surface states in the electronic structure of pyrochlore iridates, Phys. Rev. B **83**, 205101 (2011).

[18] Z. Wang, Y. Sun, X.-Q. Chen, C. Franchini, G. Xu, H. M. Weng, X. Dai, and Z. Fang, Dirac semimetal and topological phase transitions in A_3Bi (A = Na, K, Rb), Phys. Rev. B **85**, 195320 (2012).

[19] Z. K. Liu, B. Zhou, Y. Zhang, Z. J. Wang, H. M. Weng, D. Prabhakaran, S.-K. Mo, Z. X. Shen, Z. Fang, X. Dai, Z. Hussain, and Y. L. Chen, Discovery of a three-dimensional topological Dirac semimetal Na_3Bi, Science **343**, 864 (2014).

[20] M. Neupane, S.-Y. Xu, R. Sankar, N. Alidoust, G. Bian, C. Liu, I. Belopolski, T.-R. Chang, H.-T. Jeng, H. Lin, A. Bansil, F. Chou, and M. Z. Hasan, Observation of a three-dimensional topological Dirac semimetal phase in high-mobility Cd_3As_2, Nat. Commun. **5**, 3786 (2014).

[21] T. Liang, Q. Gibson, M. N. Ali, M. Liu, R. J. Cava, and N. P. Ong, Ultrahigh mobility and giant magnetoresistance in the Dirac semimetal Cd_3As_2, Nat. Mater. **14**, 280 (2015).

[22] B. Yan and C. Felser, Topological materials: Weyl semimetals, Annu. Rev. Condens. Matter Phys. **8**, 337 (2017).

[23] S.-Y. Xu, I. Belopolski, N. Alidoust, M. Neupane, G. Bian, C. Zhang, R. Sankar, G. Chang, Z. Yuan, C.-C. Lee, S.-M. Huang, H. Zheng, J. Ma, D. S. Sanchez, B. Wang, A. Bansil, F. Chou, P. P. Shibayev, H. Lin, S. Jia *et al.*, Discovery of a

Weyl fermion semimetal and topological Fermi arcs, Science **349**, 613 (2015).

[24] B. Q. Lv, H. M. Weng, B. B. Fu, X. P. Wang, H. Miao, J. Ma, P. Richard, X. C. Huang, L. X. Zhao, G. F. Chen, Z. Fang, X. Dai, T. Qian, and H. Ding, Experimental discovery of Weyl semimetal TaAs, Phys. Rev. X **5**, 031013 (2015).

[25] L. X. Yang, Z. K. Liu, Y. Sun, H. Peng, H. F. Yang, T. Zhang, B. Zhou, Y. Zhang, Y. F. Guo, M. Rahn, D. Prabhakaran, Z. Hussain, S. K. Mo, C. Felser, B. Yan, and Y. L. Chen, Weyl semimetal phase in the non-centrosymmetric compound TaAs, Nat. Phys. **11**, 728 (2015).

[26] S.-Y. Xu, N. Alidoust, I. Belopolski, Z. Yuan, G. Bian, T.-R. Chang, H. Zheng, V. N. Strocov, D. S. Sanchez, G. Chang, C. Zhang, D. Mou, Y. Wu, L. Huang, C.-C. Lee, S.-M. Huang, B. Wang, A. Bansil, H.-T. Jeng, T. Neupert *et al.*, Discovery of a Weyl fermion state with Fermi arcs in niobium arsenide, Nat. Phys. **11**, 748 (2015).

[27] S.-Y. Xu, C. Liu, S. K. Kushwaha, R. Sankar, J. W. Krizan, I. Belopolski, M. Neupane, G. Bian, N. Alidoust, T.-R. Chang, H.-T. Jeng, C.-Y. Huang, W.-F. Tsai, H. Lin, P. P. Shibayev, F.-C. Chou, R. J. Cava, and M. Z. Hasan, Observation of Fermi arc surface states in a topological metal, Science **347**, 294 (2015).

[28] A. A. Soluyanov, D. Gresch, Z. Wang, Q. Wu, M. Troyer, X. Dai, and B. A. Bernevig, Type-II Weyl semimetals, Nature (London) **527**, 495 (2015).

[29] A. P. Sakhya, C.-Y. Huang, G. Dhakal, X.-J. Gao, S. Regmi, B. Wang, W. Wen, R.-H. He, X. Yao, R. Smith, M. Sprague, S. Gao, B. Singh, H. Lin, S.-Y. Xu, F. Tafti, A. Bansil, and M. Neupane, Observation of Fermi arcs and Weyl nodes in a noncentrosymmetric magnetic Weyl semimetal, Phys. Rev. Mater. **7**, L051202 (2023).

[30] A. A. Burkov, M. D. Hook, and L. Balents, Topological nodal semimetals, Phys. Rev. B **84**, 235126 (2011).

[31] C. Fang, Y. Chen, H.-Y. Kee, and L. Fu, Topological nodal line semimetals with and without spin-orbital coupling, Phys. Rev. B **92**, 081201(R) (2015).

[32] C. Fang, H. M. Weng, X. Dai, and Z. Fang, Topological nodal line semimetals, Chin. Phys. B **25**, 117106 (2016).

[33] Q.-F. Liang, J. Zhou, R. Yu, Z. Wang, and H. Weng, Node-surface and node-line fermions from nonsymmorphic lattice symmetries, Phys. Rev. B **93**, 085427 (2016).

[34] S.-Y. Yang, H. Yang, E. Derunova, S. S. P. Parkin, B. Yan, and M. N. Ali, Symmetry demanded topological nodal-line materials, Adv. Phys. X **3**, 1414631 (2018).

[35] J. Hu, S.-Y. Xu, N. Ni, and Z. Mao, Transport of topological semimetals, Annu. Rev. Condens. Matter Phys. **49**, 207 (2019).

[36] D. Culcer, A. C. Keser, Y. Li, and G. Tkachov, Transport in two-dimensional topological materials: Recent developments in experiment and theory, 2D mater **7**, 022007 (2020).

[37] C. Shekhar, S. Ouardi, A. K. Nayak, G. H. Fecher, W. Schnelle, and C. Felser, Ultrahigh mobility and nonsaturating magnetoresistance in Heusler topological insulators, Phys. Rev. B **86**, 155314 (2012).

[38] C. Shekhar, A. K. Nayak, Y. Sun, M. Schmidt, M. Nicklas, I. Leermakers, U. Zeitler, Y. Skourski, J. Wosnitza, Z. Liu, Y. Chen, W. Schnelle, H. Borrmann, Y. Grin, C. Felser, and B. Yan, Extremely large magnetoresistance and ultrahigh mo-

bility in the topological Weyl semimetal candidate NbP, Nat. Phys. **11**, 645 (2015).

[39] Y. Wang, G. Luo, J. Liu, R. Sankar, N.-L. Wang, F. Chou, L. Fu, and Z. Li, Observation of ultrahigh mobility surface states in a topological crystalline insulator by infrared spectroscopy, Nat. Commun. **8**, 366 (2017).

[40] Y. He, J. Gayles, M. Yao, T. Helm, T. Reimann, V. N. Strocov, W. Schnelle, M. Nicklas, Y. Sun, G. H. Fecher, and C. Felser, Large linear non-saturating magnetoresistance and high mobility in ferromagnetic MnBi, Nat. Commun. **12**, 4576 (2021).

[41] I. A. Leahy, Y.-P. Lin, P. E. Siegfried, A. C. Treglia, J. C. W. Song, R. M. Nandkishore, and M. Lee, Nonsaturating large magnetoresistance in semimetals, Proc. Natl. Acad. Sci. USA **115**, 10570 (2018).

[42] R. Sultana, P. Neha, R. Goyal, S. Patnaik, and V. P. S. Awana, Unusual non saturating giant magneto-resistance in single crystalline Bi_2Te_3 topological insulator, J. Magn. Magn. Mater. **428**, 213 (2017).

[43] K. Shrestha, M. Chou, D. Graf, H. D. Yang, B. Lorenz, and C. W. Chu, Extremely large nonsaturating magnetoresistance and ultrahigh mobility due to topological surface states in the metallic Bi_2Te_3 topological insulator, Phys. Rev. B **95**, 195113 (2017).

[44] D. T. Son and B. Z. Spivak, Chiral anomaly and classical negative magnetoresistance of Weyl metals, Phys. Rev. B **88**, 104412 (2013).

[45] Y.-S. Jho and K.-S. Kim, Interplay between interaction and chiral anomaly: Anisotropy in the electrical resistivity of interacting Weyl metals, Phys. Rev. B **87**, 205133 (2013).

[46] X. Huang, L. Zhao, Y. Long, P. Wang, D. Chen, Z. Yang, H. Liang, M. Xue, H. Weng, Z. Fang, X. Dai, and G. Chen, Observation of the chiral-anomaly-induced negative magnetoresistance in 3D Weyl semimetal TaAs, Phys. Rev. X **5**, 031023 (2015).

[47] C.-Z. Li, L.-X. Wang, H. Liu, J. Wang, Z.-M. Liao, and D.-P. Yu, Giant negative magnetoresistance induced by the chiral anomaly in individual Cd_3As_2 nanowires, Nat. Commun. **6**, 10137 (2015).

[48] Q. Li, D. E. Kharzeev, C. Zhang, Y. Huang, I. Pletikosić, A. V. Fedorov, R. D. Zhong, J. A. Schneeloch, G. D. Gu, and T. Valla, Chiral magnetic effect in $ZrTe_5$, Nat. Phys. **12**, 550 (2016).

[49] F. Balduini, A. Molinari, L. Rocchino, V. Hasse, C. Felser, M. Sousa, C. Zota, H. Schmid, A. G. Grushin, and B. Gotsmann, Intrinsic negative magnetoresistance from the chiral anomaly of multifold fermions, Nat. Commun. **15**, 6526 (2024).

[50] L. M. Schoop, M. N. Ali, C. Straßer, A. Topp, A. Varykhalov, D. Marchenko, V. Duppel, S. S. P. Parkin, B. V. Lotsch, and C. R. Ast, Dirac cone protected by non-symmorphic symmetry and three-dimensional Dirac line node in ZrSiS, Nat. Commun. **7**, 11696 (2016).

[51] M. Neupane, I. Belopolski, M. M. Hosen, D. S. Sanchez, R. Sankar, M. Szlawska, S.-Y. Xu, K. Dimitri, N. Dhakal, P. Maldonado, P. M. Oppeneer, D. Kaczorowski, F. C. Chou, M. Z. Hasan, and T. Durakiewicz, Observation of topological nodal fermion semimetal phase in ZrSiS, Phys. Rev. B **93**, 201104(R) (2016).

[52] A. Topp, J. M. Lippmann, A. Varykhalov, V. Duppel, B. V. Lotsch, C. R. Ast, and L. M. Schoop, Non-symmorphic band

degeneracy at the Fermi level in ZrSiTe, New J. Phys. **18**, 125014 (2016).

[53] J. Hu, Z. Tang, J. Liu, X. Liu, Y. Zhu, D. Graf, K. Myhro, S. Tran, C. N. Lau, J. Wei, and Z. Mao, Evidence of topological nodal-line fermions in ZrSiSe and ZrSiTe, Phys. Rev. Lett. **117**, 016602 (2016).

[54] Q. Xu, Z. Song, S. Nie, H. Weng, Z. Fang, and X. Dai, Two-dimensional oxide topological insulator with iron-pnictide superconductor LiFeAs structure, Phys. Rev. B **92**, 205310 (2015).

[55] L. Y. Cao, M. Yang, L. Wang, Y. Li, B. X. Gao, L. Wang, J. L. Liu, A. F. Fang, Y. G. Shi, and R. Y. Chen, Optical study of the topological materials LnSbTe (Ln = La, Ce, Sm, Gd), Phys. Rev. B **106**, 245145 (2022).

[56] T. H. Salters, J. Colagiuri, A. K. Liston, J. Leeman, T. Berry, and L. M. Schoop, Synthesis and stability phase diagram of topological semimetal family LnSb$_x$Te$_{2-x-\delta}$, Chem. Mater. **36**, 11873 (2024).

[57] Y. Wang, Y. Qian, M. Yang, H. Chen, C. Li, Z. Tan, Y. Cai, W. Zhao, S. Gao, Y. Feng, S. Kumar, E. F. Schwier, L. Zhao, H. Weng, Y. Shi, G. Wang, Y. Song, Y. Huang, K. Shimada, Z. Xu *et al.*, Spectroscopic evidence for the realization of a genuine topological nodal-line semimetal in LaSbTe, Phys. Rev. B **103**, 125131 (2021).

[58] L. M. Schoop, A. Topp, J. Lippmann, F. Orlandi, L. Müchler, M. G. Vergniory, Y. Sun, A. W. Rost, V. Duppel, M. Krivenkov, S. Sheoran, P. Manuel, A. Varykhalov, B. Yan, R. K. Kremer, C. R. Ast, and B. V. Lotsch, Tunable Weyl and Dirac states in the nonsymmorphic compound CeSbTe, Sci. Adv. **4**, eaar2317 (2018).

[59] D. Yuan, D. Huang, X. Ma, X. Chen, H. Ren, Y. Zhang, W. Feng, X. Zhu, B. Wang, X. He, J. Wu, S. Tan, Q. Hao, Q. Zhang, Y. Liu, Q. Liu, Z. Liu, C. Cao, Q. Chen, and X. Lai, Observation of Dirac nodal line states in topological semimetal candidate PrSbTe, Phys. Rev. B **109**, 045113 (2024).

[60] S. Regmi, I. B. Elius, A. P. Sakhya, M. Sprague, M. I. Mondal, N. Valadez, V. Buturlim, K. Booth, T. Romanova, A. Ptok, D. Kaczorowski, and M. Neupane, Electronic structure in a rare-earth based nodal-line semimetal candidate PrSbTe, Phys. Rev. Mater. **8**, L041201 (2024).

[61] S. Regmi, R. Smith, A. P. Sakhya, M. Sprague, M. I. Mondal, I. B. Elius, N. Valadez, A. Ptok, D. Kaczorowski, and M. Nepane, Observation of gapless nodal-line states in NdSbTe, Phys. Rev. Mater. **7**, 044202 (2023).

[62] S. Regmi, G. Dhakal, F. C. Kabeer, N. Harrison, F. Kabir, A. P. Sakhya, K. Gofryk, D. Kaczorowski, P. M. Oppeneer, and M. Neupane, Observation of multiple nodal lines in SmSbTe, Phys. Rev. Mater. **6**, L031201 (2022).

[63] K. Pandey, D. Mondal, J. W. Villanova, J. Roll, R. Basnet, A. Wegner, G. Acharya, M. R. U. Nabi, B. Ghosh, J. Fujii, J. Wang, B. Da, A. Agarwal, I. Vobornik, A. Politano, S. Barraza-Lopez, and J. Hu, Magnetic topological semimetal phase with electronic correlation enhancement in SmSbTe, Adv. Quantum Technol. **4**, 2100063 (2021).

[64] M. M. Hosen, G. Dhakal, K. Dimitri, P. Maldonado, A. Aperis, F. Kabir, C. Sims, P. Riseborough, P. M. Oppeneer, D. Kaczorowski, T. Durakiewicz, and M. Neupane, Discovery of topological nodal-line fermionic phase in a magnetic material GdSbTe, Sci. Rep. **8**, 13283 (2018).

[65] F. Gao, J. Huang, W. Ren, H. Wu, M. An, X. Wu, L. Zhang, T. Yang, A. Wang, Y. Chai, X. Zhao, T. Yang, B. Li, and Z. Zhang, Magnetic and magnetotransport properties of the magnetic topological nodal-line semimetal TbSbTe, Adv. Quantum Technol. **6**, 2200163 (2023).

[66] I. B. Elius, J. F. Casey, S. Regmi, V. Buturlim, A. P. Sakhya, M. Sprague, M. I. Mondal, N. Valadez, A. K Kumay, J. Scrivens, Y. Venkateswara, S. Dan, T. Romanova, A. K Pathak, K. Gofryk, A. Ptok, D. Kaczorowski, and M. Neupane, Electronic structure of a nodal line semimetal candidate TbSbTe, Phys. Rev. Mater. **9**, 064202 (2025).

[67] N. Valadez, I. B. Elius, D. James, P. Radanovich, T. Romanova, S. Elgalal, G. Chajewski, F. Mesple, E. Thompson, K. T. Chu, M. Yankowitz, A. Ptok, D. Kaczorowski, and M. Neupane, Low-lying electronic structure of rare-earth based topological nodal line semimetal candidate DySbTe, Phys. Rev. B **112**, 155148 (2025).

[68] S. Yue, Y. Qian, M. Yang, D. Geng, C. Yi, S. Kumar, K. Shimada, P. Cheng, L. Chen, Z. Wang, H. Weng, Y. Shi, K. Wu, and B. Feng, Topological electronic structure in the antiferromagnet HoSbTe, Phys. Rev. B **102**, 155109 (2020).

[69] R. Singha, A. Pariari, B. Satpati, and P. Mandal, Magnetotransport properties and evidence of a topological insulating state in LaSbTe, Phys. Rev. B **96**, 245138 (2017).

[70] B. Lv, J. Chen, L. Qiao, J. Ma, X. Yang, M. Li, M. Wang, Q. Tao, and Z.-A. Xu, Magnetic and transport properties of low-carrier-density Kondo semimetal CeSbTe, J. Phys.: Condens. Matter **31**, 355601 (2019).

[71] K. Pandey, R. Basnet, A. Wegner, G. Acharya, Md Rafique Un Nabi, J. Liu, J. Wang, Y. K. Takahashi, B. Da, and J. Hu, Electronic and magnetic properties of the topological semimetal candidate NdSbTe, Phys. Rev. B **101**, 235161 (2020).

[72] R. Sankar, I. P. Muthuselvam, K. Rajagopal, K. Ramesh Babu, G. S. Murugan, K. S. Bayikadi, K. Moovendaran, C. T. Wu, and G.-Y. Guo, Anisotropic magnetic properties of nonsymmorphic semimetallic single crystal NdSbTe, Crys. Growth Des. **20**, 6585 (2020).

[73] R. Sankar, I. P. Muthuselvam, K. R. Babu, G. S. Murugan, K. Rajagopal, R. Kumar, T.-C. Wu, C.-Y. Wen, W.-L. Lee, G.-Y. Guo, and F.-C. Chou, Crystal growth and magnetic properties of topological nodal-line semimetal GdSbTe with antiferromagnetic spin ordering, Inorg. Chem. **58**, 11730 (2019).

[74] F. Gao, J. Huang, W. Ren, M. Li, H. Wang, T. Yang, B. Li, and Z. Zhang, Magnetic and transport properties of the topological compound DySbTe, Phys. Rev. B **105**, 214434 (2022).

[75] M. Yang, Y. Qian, D. Yan, Y. Li, Y. Song, Z. Wang, C. Yi, H. L. Feng, H. Weng, and Y. Shi, Magnetic and electronic properties of a topological nodal line semimetal candidate: HoSbTe, Phys. Rev. Mater. **4**, 094203 (2020).

[76] R. Singha, T. H. Salters, S. Teicher, S. M. Lei, J. F. Khoury, N. P. Ong, and L. M. Schoop, Evolving devil's staircase magnetization from tunable charge density waves in non-symmorphic Dirac semimetals, Adv. Mater. **33**, 2103476 (2021).

[77] P. Li, B. Lv, Y. Fang, W. Guo, Z. Wu, Y. Wu, D. Shen, Y. Nie, L. Petaccia, C. Cao, Z.-A. Xu, and Y. Liu, Charge density wave and weak Kondo effect in a Dirac semimetal CeSbTe, Sci. China Phys. Mech. Astron. **64**, 237412 (2021).

[78] N. Shumiya, J.-X. Yin, G. Chang, M. Yang, S. Mardanya, T.-R. Chang, H. Lin, M. S. Hossain, Y.-X. Jiang, T. A. Cochran,

Q. Zhang, X. P. Yang, Y. Shi, and M. Z. Hasan, Evidence for electronic signature of a magnetic transition in the topological magnet HoSbTe, Phys. Rev. B **106**, 035151 (2022).

[79] M. Kriener, T. Koretsune, R. Arita, Y. Tokura, and Y. Taguchi, Enhancement of the thermoelectric figure of merit in the Dirac semimetal Cd_3As_2 by band-structure and -filling control, Sci. Tech. Adv. Mat. **25**, 2412971 (2024).

[80] S. Lei, V. Duppel, J. M. Lippmann, J. Nuss, B. V. Lotsch, and L. M. Schoop, Charge density waves and magnetism in topological semimetal candidates $GdSb_xTe_{2-x-\delta}$, Adv. Quantum Technol. **2**, 1900045 (2019).

[81] S. Lei, S. M. L. Teicher, A. Topp, K. Cai, J. Lin, G. Cheng, T. H. Salters, F. Rodolakis, J. L. McChesney, S. Lapidus, N. Yao, M. Krivenkov, D. Marchenko, A. Varykhalov, C. R. Ast, R. Car, J. Cano, M. G. Vergniory, N. P. Ong, and L. M. Schoop, Band engineering of Dirac semimetals using charge density waves, Adv. Mater. **33**, 2101591 (2021).

[82] S. Lei, A. Saltzman, and L. M. Schoop, Complex magnetic phases enriched by charge density waves in the topological semimetals $GdSb_xTe_{2-x-\delta}$, Phys. Rev. B **103**, 134418 (2021).

[83] T. H. Salters, F. Orlandi, T. Berry, J. F. Khoury, E. Whittaker, P. Manuel, and L. M. Schoop, Charge density wave-templated spin cycloid in topological semimetal, Phys. Rev. Mater. **7**, 044203 (2023).

[84] E. DiMasi, B. Foran, M. C. Aronson, and S. Lee, Stability of charge-density waves under continuous variation of band filling in $LaTe_{2-x}Sb_x$ ($0 \leqslant x \leqslant 1$), Phys. Rev. B **54**, 13587 (1996).

[85] K. Momma and F. Izumi, VESTA 3 for three-dimensional visualization of crystal, volumetric and morphology data, J. Appl. Cryst. **44**, 1272 (2011).

[86] P. Blaha, K. Schwarz, F. Tran, R. Laskowski, G. K. H. Madsen, and L. D. Marks, WIEN2k: An APW lo program for calculating the properties of solids, J. Chem. Phys. **152**, 074101 (2020).

[87] A. Kokalj, Computer graphics and graphical user interfaces as tools in simulations of matter at the atomic scale, Comp. Mater. Sci. **28**, 155 (2003).

[88] Q. Wu, S. Zhang, H. Song, M. Troyer, and A. A. Soluyanov, WannierTools : An open-source software package for novel topological materials, Comp. Phys. Commun. **224**, 405 (2018).

[89] J. Kuneš, R. Arita, P. Wissgott, A. Toschi, H. Ikeda, and K. Held, Wien2wannier: From linearized augmented plane waves to maximally localized wannier functions, Comp. Phys. Commun. **181**, 1888 (2010).

[90] G. Pizzi, V. Vitale, R. Arita, S. Blügel, F. Freimuth, G. Géranton, M. Gibertini, D. Gresch, C. Johnson, T. Koretsune, J. Ibañez-Azpiroz, H. Lee, J. Lihm, D. Marchand, A. Marrazzo, Y. Mokrousov, J. I. Mustafa, Y. Nohara, Y. Nomura, L. Paulatto *et al.*, WANNIER90 as a community code: new features and applications, J. Phys.: Condens. Matter **32**, 165902 (2020).

[91] See Supplemental Material at http://link.aps.org/supplemental/10.1103/jmlt-7q5r for auxiliary results supporting or used in the discussion of this article, including first-principles calculation results, enlarged views, and comparisons of crystal-structure refinement R values: (i) electronic structures of Te-rich $LaSb_{1-x}Te_{1+x}$ ($x = 0$, 0.25, 0.5, and 1.0), calculated using the virtual crystal approximation; (ii) crystal-structure refinement R values of 2c-LaSbTe and YSbTe; (iii) extended views of the electronic structures of 2c-LaSbTe; (iv) extended views of the electronic structures of $2c$-YSb_1Te_1 and the corresponding density of states; (v) first-principles calculation results of 2c-structured $YSb_{1.3}Te_{0.7}$; (vi) first-principles calculation results of 1c-structured $YSb_{0.9}Te_{1.1}$; and (vii) first-principles calculation results of ZrSnTe. The crystallographic information files for $LaSb_{1.2}Te_{0.8}$, $YSb_{0.9}Te_{1.1}$, YSb_1Te_1, and $YSb_{1.3}Te_{0.7}$ used for the first-principles calculations are also provided as separate files.

[92] A. Kikuchi, Electronic structure of lanthan ditellurides, J. Phys. Soc. Jpn. **67**, 1308 (1998).

[93] H. Sakai, H. Fujimura, S. Sakuragi, M. Ochi, R. Kurihara, A. Miyake, M. Tokunaga, T. Kojima, D. Hashizume, T. Muro, K. Kuroda, Takeshi Kondo, T. Kida, M. Hagiwara, K. Kuroki, M. Kondo, K. Tsuruda, H. Murakawa, and N. Hanasaki, Bulk quantum hall effect of spin-valley coupled Dirac fermions in the polar antiferromagnet $BaMnSb_2$, Phys. Rev. B **101**, 081104(R) (2020).

[94] J. Bannies, M. Michiardi, H.-H. Kung, S. Godin, J. W. Simonson, M. Oudah, M. Zonno, S. Gorovikov, S. Zhdanovich, I. S. Elfimov, A. Damascelli, and M. C. Aronson, Electronically-driven switching of topology in LaSbTe, arXiv:2407.08798.

[95] A. Topp, R. Queiroz, A. Grüneis, L. Müchler, A. W. Rost, A. Varykhalov, D. Marchenko, M. Krivenkov, F. Rodolakis, J. L. McChesney, B. V. Lotsch, L. M. Schoop, and C. R. Ast, Surface floating 2D bands in layered nonsymmorphic semimetals: ZrSiS and related compounds, Phys. Rev. X **7**, 041073 (2017).

[96] L. Muechler, A. Topp, R. Queiroz, M. Krivenkov, A. Varykhalov, J. Cano, C. R. Ast, and L. M. Schoop, Modular arithmetic with nodal lines: Drumhead surface states in ZrSiTe, Phys. Rev. X **10**, 011026 (2020).

[97] C. Chen, X. Xu, J. Jiang, S. C. Wu, Y. P. Qi, L. X. Yang, M. X. Wang, Y. Sun, N. B. M. Schröter, H. F. Yang, L. M. Schoop, Y. Y. Lv, J. Zhou, Y. B. Chen, S. H. Yao, M. H. Lu, Y. F. Chen, C. Felser, B. H. Yan, Z. K. Liu *et al.*, Dirac line nodes and effect of spin-orbit coupling in the nonsymmorphic critical semimetals MSiS (M = Hf, Zr), Phys. Rev. B **95**, 125126 (2017).

[98] B. Bradlyn, L. Elcoro, J. Cano, M. G. Vergniory, Z. Wang, C. Felser, M. i. Aroyo, and B. A. Bernevig, Topological quantum chemistry, Nature (London) **547**, 298 (2017).

[99] C. Guo, L. Hu, C. Putzke, J. Diaz, X. Huang, K. Manna, F. -R. Fan, C. Shekhar, Y. Sun, C. Felser, Ch Liu, B. A. Bernevig, and P. J. W. Moll, Quasi-symmetry-protected topology in a semimetal, Nat. Phys. **18**, 813 (2022).

[100] K. Pandey, L. Sayler, R. Basnet, J. Sakon, F. Wang, and J. Hu, Crystal Growth and Electronic Properties of LaSbSe, Crystals **12**, 1663 (2022).